Journal of The Electrochemical Society

Quasi-Isothermal External Short Circuit Tests Applied to Lithium-Ion Cells: Part II. Modeling and Simulation

Quasi-Isothermal External Short Circuit Tests Applied to Lithium-Ion Cells: Part II. Modeling and Simulation

Alexander Rheinfeld,[1,*,z] Johannes Sturm,[1] Andreas Noel,[1] Jörn Wilhelm,[1] Akos Kriston,[2,] Andreas Pfrang,[2] and Andreas Jossen[1]**

[1] *Institute for Electrical Energy Storage Technology, Technical University of Munich (TUM), D-80333 Munich, Germany*

[2] *European Commission, Joint Research Centre (JRC), Directorate for Energy, Transport and Climate, Energy Storage Unit, 1755 LE Petten, The Netherlands*

Measurement data gained from quasi-isothermal external short circuit tests on single-layered pouch-type Li-ion cells presented in the first part of this combined work was used to validate a well-known homogenized physical-chemical model for different electrode loadings, cell temperatures, initial cell voltages, and external short circuit resistances. Accounting for diffusion-limited reaction kinetics, effective solid phase diffusion coefficients, and one representative active material particle size within each electrode, the model is capable of describing the experimentally observed characteristic change in magnitudes of current and heat generation rate throughout the short circuit. Underlying mechanisms for the observed characteristics are studied by evaluating the predicted concentration distribution across the electrodes and separator and by calculating the cell polarization due to ohmic losses, diffusion processes, and reaction kinetics. The importance of mass transport in the solid and liquid phase limiting reaction kinetics is discussed and evaluated in the context of a sensitivity analysis. Concentration dependent transport properties, electrode tortuosity, particle size, and electrode energy density are affecting different stages of a short circuit. Simulation results suggest a strong impact of electrode design on the short circuit dynamics allowing for an optimization regarding a cell's energy and power characteristics whilst guaranteeing a high short circuit tolerance.

 [DOI: 10.1149/2.0071902jes]

Manuscript submitted October 31, 2018; revised manuscript received December 11, 2018. Published January 15, 2019.

To date, lithium-ion batteries are the energy storage technology of choice for applications requiring a high gravimetric and volumetric energy density. Whilst the battery's energy density defines the runtime of a mobile device or the driving range of an electric vehicle at a given battery weight or volume, the battery's rate capability sets the limits for high performance scenarios such as acceleration, recuperation, and fast charging. Even though the work presented here focuses on Li-ion batteries, this circumstance is not restricted to this chemistry alone but holds true for all battery types. Increasing a battery's energy density can be achieved by applying advanced active materials[1] and by maximizing the active material content compared to the battery's electrochemically inactive components such as current collectors, separator, binder, and conductive agents.[2,3] An increase in the share of active materials can be achieved e.g. by designing dense[4] and/or thick electrodes[5] which, however, generally comes with a trade-off regarding a battery's rate capability.[6] This implies that batteries that are designed for applications requiring a high energy density can often supply this energy level only at comparably low currents. For mobile and automotive applications demanding ever increasing energy densities, this mostly does not pose a major problem during discharge as the battery is generally exposed to rather low currents on average.[7] However, with an increasing demand for fast charging, especially Li-ion batteries with a high energy density often do not allow for high continuous charge currents due to large local overpotentials occurring during operation resulting in anode potentials below 0 V vs. Li/Li^+ and consequently lithium-plating. In contrast, batteries that can deliver a sufficiently high power capability also at elevated currents, mostly suffer a reduced energy density. To overcome this trade-off with a given combination of active materials, electrochemically engineered electrodes are recently gaining more attention in the community. By adapting the morphology of the active material particles and electrodes as a whole, the rate capability can be improved due to reduced overpotentials based on ion movement within the cell's solid and liquid components.[1,8]

With increasing the total electrical energy content stored at a constant weight or volume of a battery, also the thermal energy content is increased which poses a certain risk in case of a battery failure. By employing active materials allowing for an increase in energy density of Li-ion batteries such as nickel-rich layered oxides, the thermal stability of the battery's active components is substantially reduced.[9–11] By adapting the morphology of the active materials and electrodes to also guarantee a high rate capability of the battery, this safety risk is even further increased. With an electrode morphology allowing for a high rate capability of a battery during normal operation, also the current and heat generation rate occurring during a short circuit are increased leading to an accelerated heat up with potential safety risks.[12] Furthermore, by employing active materials with a small active material particle size enhancing rate capability due to reduced solid phase diffusion based and reaction related overpotentials, the thermal stability is considerably compromised resulting from the decreased diffusion path and increased reaction surface area.[13,14]

A substantial number of experimental results,[5,6,15–18] simulation data,[19–22] and a combination of both[8,23–31] has been reported in literature to understand rate limiting effects within and beyond the designated operating window of Li-ion batteries at predominantly constant currents. However, only little data has been presented so far to adequately evaluate the underlying mechanisms of a battery's electrical and electrochemical response during abusive short circuit conditions.[12,32–35] With Li-ion battery short circuits being often synonymously used to refer to a worst-case internal short circuit within a cell, the focus of published work dealing with test development and experiments[36–39] as well as modeling and simulation[40–43] or both[44–53] has been predominantly focused on this event. Besides the recently increasing attention toward mechanical abuse conditions,[54] safety related modeling and simulation is mainly related the thermal response of a battery describing runaway related processes resulting from internal or external heat sources.[55–58] Even though short circuits are often considered as such a trigger heat source, the underlying mechanisms resulting in a certain current, electrode polarization, and consequently heat generation rate are mostly not further investigated.

Previous experimental results suggest a transient change of rate limiting mechanisms occurring during short circuit events.[12,32] With a cell delivering the maximum current possible at every moment of the discharge, hard external short circuits can be considered as the ultimate rate capability test of a cell. Therefore, previous work studying rate capability of materials,[27] electrodes,[5,6,15–18,27,31] and

*Electrochemical Society Student Member.
**Electrochemical Society Member.
ᶻE-mail: alexander.rheinfeld@tum.de

cells[19–26,28–30] identifying reaction kinetics,[16,30] electron transport,[6] Li-ion transport in the solid[25,27,31] or liquid phase[5,15–18,20,23,24,29–31] or a combination[16,19,21,22,26,28,31] as the dominating rate limiting mechanism depending on the size of the active material particles,[17,19,27] electrode thickness[5,15,16,19–21,23,24,26,29–31] or electrode morphology,[6,18,20,22,31] are considered as the basis for the work presented here. Previous results suggest that a battery which exhibits a balanced contribution of resistances based on mass and charge transport as well as reaction kinetics shows a maximized rate capability for a set of materials and morphologies.[19,23] However, this might also imply that a battery which is optimized in terms of its rate capability also poses an increased risk when exposed to a short circuit.

Within this work, previously published experimental data of quasi-isothermal external short circuit tests applied to single-layered pouch-type Li-ion cells[12] is used to validate a well-known, widely accepted and applied physical-chemical modeling approach[59,60] at very high currents. The impact of varying electrode morphologies is studied for Li-ion cells comprising graphite anodes and $LiNi_{1/3}Co_{1/3}Mn_{1/3}O_2$ cathodes (NCM-111, in the following written as NMC-111) with nominal electrode loadings of 1 mAh cm^{-2} (i.e. high power loading, HP), 2 mAh cm^{-2} (i.e. balanced loading, BA), and 3.5 mAh cm^{-2} (i.e. high energy loading, HE). By further varying the cell's temperature, its initial voltage or initial state of charge (SoC), as well as the external short circuit resistance, the model is evaluated for its capability of simulating differing boundary and starting conditions. With the aid of the validated model, experimentally observed stages in current and heat generation rate during external short circuits are correlated to reaction kinetics as well as to mass and charge transport based processes and limitations within the electrodes. Based on the contribution of each mechanism to the observed overpotential,[26] a sensitivity analysis is carried out, on the one hand, to study the influence of the material's inherent transport properties on the transient short circuit behavior and, on the other hand, to evaluate the impact of electrode morphology which defines not only the effective transport length for electrons and ions but which also sets the limits for the cell's energy density.

Modeling

Within this section, the chosen modeling approach to describe the electrochemical response of Li-ion cells exposed to external short circuits is presented. In the first part, means of increasing the numerical stability when solving the model are evaluated and discussed, based on previously published findings. In the second part of the section, the model parameters used for describing the investigated cells are presented.

Diffusion limited currents.—Based on Newman's physical-chemical model,[59,60] cell-internal processes occurring in Li-ion batteries during both operation and resting periods can be reliably described, which has been demonstrated in the past for a manifold of electrode materials and load profiles. Recently, the applicability of the modeling approach to also describe large current densities occurring during abusive short circuit events has been discussed[33,34] but not validated. Provided that no further phenomena such as a possible deviation from electro-neutrality (at high currents or low salt concentrations[61]), solvent convection (at high salt concentrations and concentration gradients[62]), salt precipitation (at high salt concentrations[28]) or thermal decomposition reactions (at high temperatures[55,63,64]) are dominating the cell behavior and as long as the model equations can be solved without facing numerical issues, in theory the model should be also valid for describing a cell's response during hard external short circuit tests. Based on the theories of porous electrodes and concentrated solutions,[60] the applied pseudo two-dimensional (p2D) model accounts for a material balance and Ohm's law within both solid and liquid components as well as a charge balance based on Butler-Volmer reaction kinetics which can be summarized in five partial differential equations.

In order to guarantee a numerically stable operation of the model even at very high currents whilst following a physical concept, the Newman group recently adapted the original model by including an additional term in the Butler-Volmer equation resembling a diffusion limited depletion of Li-ions within the radial direction of the pores.[33,34] With this modification, the original Dualfoil model is reported to successfully run at virtually all currents as a complete depletion of Li-ions within the electrolyte can be efficiently suppressed.

The tendency of the original Newman model to develop such numerical issues is based on the nature of the applied Butler-Volmer equation, combined with the calculated exchange current density i_0 (A m^{-2}) as suggested by the Newman group[59,65] to derive the pore wall flux j_n (mol m^{-2} s^{-1})

$$j_n = \frac{i_0}{F}\left[\exp\left(\frac{\alpha_a F}{RT}\eta\right) - \exp\left(\frac{\alpha_c F}{RT}\eta\right)\right] \quad [1]$$

whereas α_a and α_c represent the anodic and cathodic charge-transfer coefficients of the reaction (with $\alpha_a + \alpha_c = 1$) following the reaction overpotential η (V). F describes Faraday's constant (96485 C mol^{-1}), R the universal gas constant (8.314 J mol^{-1}K^{-1}) and T the absolute temperature in Kelvin. To be able to include experimentally measured half-cell equilibrium potentials E_{eq} (V) in the Butler-Volmer equation, η is generally written in the form[59,65]

$$\eta = \Phi_s - \Phi_l - E_{eq} \quad [2]$$

based on the potentials Φ_s and Φ_l (V) in the solid and liquid phase of the electrodes. The exchange current density is commonly calculated as[59,65]

$$i_0 = F k_c^{\alpha_a} k_a^{\alpha_c} \left(\frac{c_l}{c_{l,\,ref}}\right)^{\alpha_a} \left(c_{s,\,max} - c_{s,\,surf}\right)^{\alpha_a} \left(c_{s,\,surf}\right)^{\alpha_c} \quad [3]$$

whereas k_a and k_c represent the anodic and cathodic reaction rate constants (m s^{-1}), c_l describes the salt concentration in the liquid electrolyte (mol m^{-3}) with a reference concentration $c_{l,\,ref}$ of 1 mol m^{-3}, and $c_{s,\,max}$ and $c_{s,\,surf}$ represent the maximum Li-ion concentration and surface concentration of the solid active material particles.

As previously stated by Latz and Zausch,[66] the commonly applied combination of Eqs. 1, 2, and 3 in Li-ion battery modeling struggles to describe a cell's behavior as soon as the liquid or solid phase is completely depleted at the reaction site (i.e. $c_l = 0$ or $c_{s,\,surf} = 0$), or the surface concentration of the active material particles approaches the maximum solid phase concentration (i.e. $c_{s,\,max} - c_{s,\,surf} = 0$). At these extremes, the exchange current density approaches 0 whilst the measured half-cell potential approaches a finite value. This singular behavior leads to numerical issues when calculating the pore-wall flux. As a result, the discharge process of a cell with a fully lithiated anode could simply not be described. Furthermore, a deep discharge of a cell during abusive short circuits would also result in numerical issues. To overcome this problem, Latz and Zausch suggested a reformulation of the Butler-Volmer equation based on nonequilibrium thermodynamics resulting in pre-exponential factors for both the anodic and cathodic reaction differing from the original equation.[66]

The approach suggested by the Newman group[33,34] aims at modifying only the cathodic reaction by including an additional pre-exponential factor in the original Butler-Volmer equation based on the concept of a limiting current density i_{lim}. For the investigated short circuit conditions, the cathodic reaction in the positive electrode was modified in order to avoid c_l approaching a complete depletion or becoming even negative.

$$i_n = j_n F = \frac{i_0\left[\exp\left(\frac{\alpha_a F}{RT}\eta\right) - \exp\left(\frac{\alpha_c F}{RT}\eta\right)\right]}{1 - \frac{i_0}{i_{lim}}\exp\left(\frac{\alpha_c F}{RT}\eta\right)} \quad [4]$$

The limiting current density i_{lim} in Eq. 4 is assumed to represent a diffusion limitation in the liquid electrolyte, which is fundamentally related to the thickness of the Nernst diffusion layer δ_l (m) at the interface between the liquid electrolyte and the surface of the solid active material particles.[67] Assuming a linear concentration profile within the Nernst diffusion layer separating the bulk electrolyte (c_l) from the reaction site ($c_{l,\,surf}$), the absolute value of the limiting current

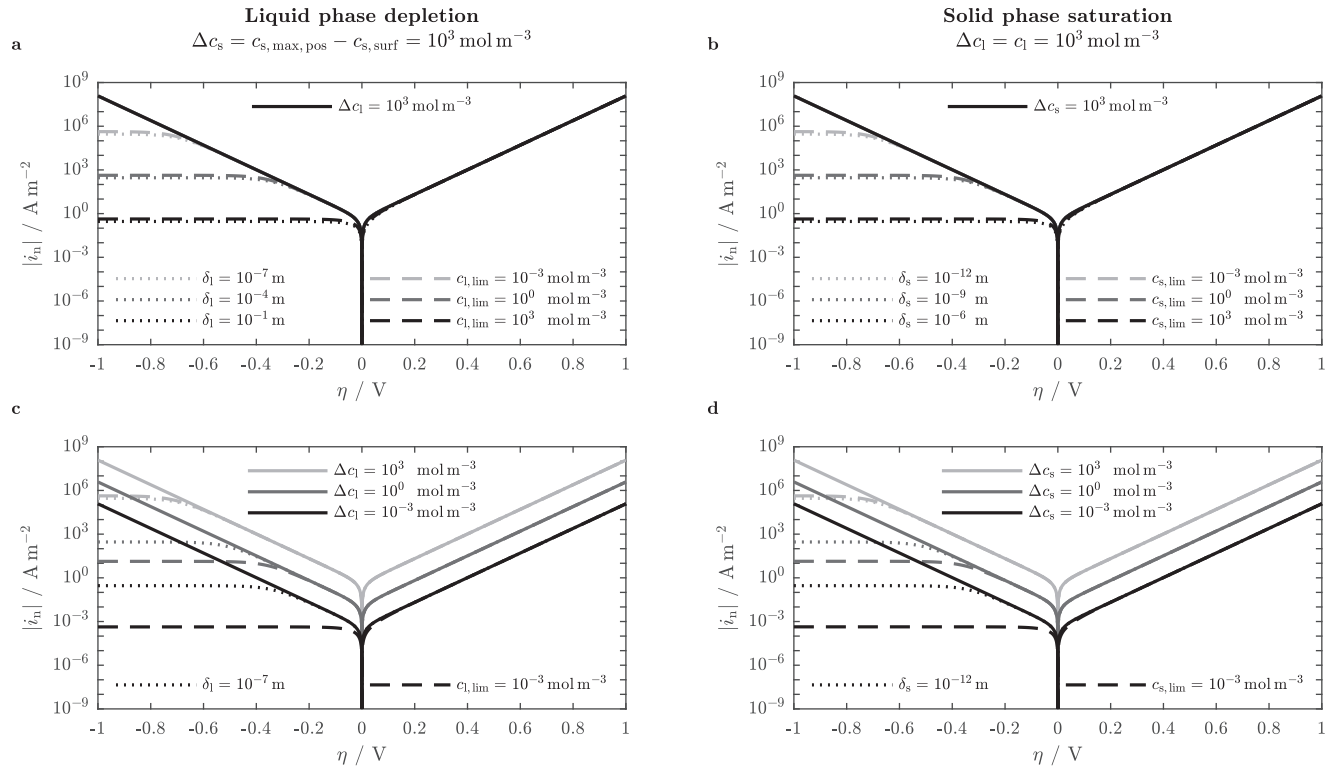

Figure 1. Influence of diffusion limited currents based on the Nernst diffusion layer thickness δ_i and limiting concentration $c_{i,\,\mathrm{lim}}$ in the liquid (i = l; left: a and c) and solid phase (i = s; right: b and d) on the reaction overpotential of the positive electrode at varying levels of limitation δ_i and $c_{i,\,\mathrm{lim}}$ and constant concentrations (top: a and b) as well as at varying concentrations and constant levels of limitation δ_i and $c_{i,\,\mathrm{lim}}$ (bottom: c and d) for $T = 25^{\circ}\mathrm{C}$, $\alpha_\mathrm{a} = \alpha_\mathrm{c} = 0.5$, $k_\mathrm{a} = k_\mathrm{c} = k = 2 \times 10^{-11}\,\mathrm{m\,s^{-1}}$, $c_{\mathrm{s,\,max}} = 50000\,\mathrm{mol\,m^{-3}}$, $D_\mathrm{l} = 0.3 \times 10^{-9}\,\mathrm{m^2\,s^{-1}}$, $D_\mathrm{s} = 0.3 \times 10^{-14}\,\mathrm{m^2\,s^{-1}}$, $c_{\mathrm{s,\,surf}} = 49000\,\mathrm{mol\,m^{-3}}$ (a and c), and $c_\mathrm{l} = 1000\,\mathrm{mol\,m^{-3}}$ (b and d).

density can be estimated via Fick's law[67]

$$|i_\mathrm{lim}| = F D_\mathrm{l} \frac{c_\mathrm{l} - c_{\mathrm{l,\,surf}}}{\delta_\mathrm{l}} = F D_\mathrm{l} \frac{\Delta c_\mathrm{l}}{\delta_\mathrm{l}} \qquad [5]$$

whereas D_l represents the salt diffusion coefficient of solvated Li-ions in the liquid electrolyte ($\mathrm{m^2\,s^{-1}}$) and $c_{\mathrm{l,\,surf}}$ approaches 0 in this case, so that $\Delta c_\mathrm{l} = c_\mathrm{l}$. With cathodic currents being negative by definition, i_lim also needs to be negative resulting in

$$i_\mathrm{n} = \frac{i_0 \left[\exp\left(\frac{\alpha_\mathrm{a} F}{RT}\eta\right) - \exp\left(\frac{\alpha_\mathrm{c} F}{RT}\eta\right)\right]}{1 + \frac{i_0 \delta_\mathrm{l}}{F D_\mathrm{l} \Delta c_\mathrm{l}} \exp\left(\frac{\alpha_\mathrm{c} F}{RT}\eta\right)} \qquad [6]$$

For the main purpose of guaranteeing a smooth numerical calculation whilst still following a physical concept, Eq. 6 was suggested to be simplified by assuming a constant limiting concentration $c_{\mathrm{l,\,lim}}$ as suggested by the Newman group[34]

$$c_{\mathrm{l,\,lim}} = \frac{i_0 \delta_\mathrm{l}}{F D_\mathrm{l}} \qquad [7]$$

$$i_\mathrm{n} = \frac{i_0 \left[\exp\left(\frac{\alpha_\mathrm{a} F}{RT}\eta\right) - \exp\left(\frac{\alpha_\mathrm{c} F}{RT}\eta\right)\right]}{1 + \frac{c_{\mathrm{l,\,lim}}}{\Delta c_\mathrm{l}} \exp\left(\frac{\alpha_\mathrm{c} F}{RT}\eta\right)} \qquad [8]$$

with $c_{\mathrm{l,\,lim}} \leq 1\,\mathrm{mol\,m^{-3}}$ showing the best results for the studied short circuit conditions.[34]

In the following, the suggested simplification is evaluated which has not been discussed so far. Comparing the effect of the simplified approach shown in Eq. 8 to the original concept of the Nernst diffusion layer shown in Eq. 6, δ_l is estimated based on Eq. 7.

Assuming $\alpha_\mathrm{a} = \alpha_\mathrm{c} = 0.5$ and $k_\mathrm{a} = k_\mathrm{c} = k$, whilst including Eq. 3 in Eq.7, δ_l calculates as

$$\delta_\mathrm{l} = \left(\frac{D_\mathrm{l} c_{\mathrm{l,\,lim}}}{k} \sqrt{\frac{c_{\mathrm{l,\,ref}}}{\left(c_{\mathrm{s,\,max}} - c_{\mathrm{s,\,surf}}\right) c_{\mathrm{s,\,surf}}}}\right) \frac{1}{\sqrt{c_\mathrm{l}}} \qquad [9]$$

By further considering the liquid phase diffusion coefficient, the reaction rate constant and the Li-ion concentration at the surface of the active material particles as constant, δ_l inversely follows the square root of salt concentration $\sqrt{c_\mathrm{l}}$ which itself changes with time t. This implies that with ongoing depletion of the salt concentration within the positive electrode during high discharge currents, the Nernst diffusion layer thickness increases, which in turn reduces the transfer current density. For a constant salt concentration at the reaction site (i.e. $c_{\mathrm{l,\,surf}} = 0$), the thickness of the Nernst diffusion layer can be further approximated via[67]

$$\delta_\mathrm{l} = \sqrt{\pi D_\mathrm{l} t} \qquad [10]$$

which results in

$$\delta_\mathrm{l} \sim \frac{1}{\sqrt{c_\mathrm{l}}} \sim \sqrt{t} \qquad [11]$$

By introducing a constant limiting salt concentration $c_{\mathrm{l,\,lim}}$ as previously suggested[34] and presented in Eq. 7 and Eq. 8 to simplify Eq. 6, effectively the salt concentration c_l is assumed to follow the elapsed time in an inverse fashion approaching complete depletion with t approaching ∞. Hence, applying a constant $c_{\mathrm{l,\,lim}}$ limiting reaction kinetics is equivalent to using a Nernst diffusion layer thickness δ_l which is estimated to increase in size with time as stated in Eq. 10. Confirming the plausibility of the previously suggested modification (Eq. 6) and simplification (Eq. 8) of the Butler-Volmer equation, the suggested concept is further used within this work. The effect of both Nernst diffusion layer thickness as well as a limiting concentration

in the liquid electrolyte is visualized in Fig. 1 on the left (a and c). At a given Li-ion concentration in the liquid electrolyte and at the surface of the solid active material particles, the cathodic branch of the transfer current density is reduced to decreasing limiting current densities i_{lim} with increasing δ_l in Eq. 6 and $c_{l,\text{lim}}$ in Eq. 8 (compare dotted and dashed lines to solid line in Fig. 1a). To guarantee the same levels of i_{lim}, a constant ratio between δ_l and $c_{l,\text{lim}}$ is observed. With a reduction in c_l and consequently Δc_l whilst keeping the ratio between δ_l and $c_{l,\text{lim}}$ constant, a lower limitation can be observed for Eq. 6 compared to Eq. 8 (see Fig. 1c). The relationship between δ_l and $c_{l,\text{lim}}$ is summarized in Eq. 9 showing the same levels of current limitation for varying Δc_l. For a constant $c_{l,\text{lim}}$ of 10^{-3} mol m^{-3} (1 μM) and a surface concentration of 49000 mol m^{-3} as shown in Figs. 1a and 1c, δ_l grows from approximately 68 nm to 2.1 μm and 68 μm with Δc_l decreasing from 1000 mol m^{-3} (1 M) to 1 mol m^{-3} (1 mM) and 10^{-3} mol m^{-3} (1 μM), resembling a duration of ca. 5 μs to 5 ms and 5 s according to Eq. 10. At very low salt concentrations, the calculated Nernst diffusion layer is consequently likely to exceed the pore size representing rather a diffusion limitation across the electrode thickness instead of a diffusion limitation within the pores alone.

Extensive simulation studies carried out in this work with a commercial solver (COMSOL Multiphysics 5.3a) have revealed the necessity to further consider a limited solid phase saturation and solid phase depletion within the positive and negative electrode in order to guarantee numerical stability at all times. Following a similar approach as stated in Eq. 6 and Eq. 8, the cathodic current density can be further limited by referring $c_{s,\text{lim}}$ to Δc_s which is shown in Fig. 1 on the right (b and d). Due to the several orders of magnitude smaller solid phase diffusion coefficient, the estimated δ_s is also several orders of magnitude smaller than δ_l for similar values of $c_{s,\text{lim}}$ and $c_{l,\text{lim}}$ with $\Delta c_s = c_{s,\text{max}} - c_{s,\text{surf}}$. To be able to introduce this additional pre-factor in a straightforward manner without limiting the transfer current density too much, $c_{s,\text{lim}}$ is chosen several orders of magnitude smaller than $c_{l,\text{lim}}$, showing identical simulation results compared to a limitation in the liquid phase alone, whilst guaranteeing numerical stability throughout the calculation. With this additional modification, i_n in the positive electrode calculates as

$$i_n = \frac{i_0\left[\exp\left(\frac{\alpha_a F}{RT}\eta\right) - \exp\left(\frac{\alpha_c F}{RT}\eta\right)\right]}{1 + \left(\frac{c_{l,\text{lim}}}{\Delta c_l} + \frac{c_{s,\text{lim}}}{\Delta c_s}\right)\exp\left(\frac{\alpha_c F}{RT}\eta\right)} \quad [12]$$

Analogously, the anodic transfer current density in the negative electrode is limited by considering a limited depletion of the active material particles

$$i_n = \frac{i_0\left[\exp\left(\frac{\alpha_a F}{RT}\eta\right) - \exp\left(\frac{\alpha_c F}{RT}\eta\right)\right]}{1 + \frac{c_{s,\text{lim}}}{\Delta c_s}\exp\left(\frac{\alpha_a F}{RT}\eta\right)} \quad [13]$$

with $\Delta c_s = c_{s,\text{surf}}$ in this case. An additional diffusion limitation due to a liquid phase saturation in the negative electrode was not included at this stage, as it was not necessary to guarantee numerical stability and as, to the knowledge of the authors, the maximum solubility of $LiPF_6$ in organic solvents has not been addressed so far in literature. A similar approach as suggested in this work could be used to limit the calculated pore-wall flux during fast charging whereas a cathodic diffusion limitation would be required in the negative electrode and an anodic diffusion limitation could be incorporated in the positive electrode.

All simulation studies presented in this work were carried out with $c_{l,\text{lim}} = 1$ mol m^{-3} and $c_{s,\text{lim}} = 10^{-4}$ mol m^{-3} showing the best results by improving the numerical stability whilst minimizing the impact of the suggested modifications on the simulated short circuit behavior.

All relevant model equations are summarized in Table A1 in the appendix. Based on the calculated overpotentials occurring within the cell's components[26] (see Table A2 in the appendix) and the entropic coefficients for each electrode, the irreversible and reversible heat produced throughout the short circuit can be calculated accounting for a general energy balance[68,69] which is also explained in more detail in the appendix. Because quasi-isothermal test conditions are considered in this work ($\Delta T < 1\,^{\circ}$C),[12] the temperature is regarded to be constant throughout the simulations.

Parameterization.—For parameterizing the applied p2D model, experimental results and literature data were combined. Pristine graphite and NMC-111 electrode samples were used for half-cell potential measurements vs. Li/Li$^+$. By means of a differential voltage analysis (DVA) based on both half-cell and full-cell measurements, the utilization window of the electrodes was determined for each of the HP, BA, and HE loadings. Based on micrometer screw measurements and scanning electron microscopy of pristine electrode samples and electrode samples gained from post mortem analysis,[12] the thickness of the electrodes was determined and the size of the active material particles was estimated. Entropic coefficients,[70,71] reaction rate constants,[72] charge transfer coefficients and transport parameters within both liquid electrolyte[34,73–76] and solid active material particles[27,77] as well as tortuosity values of the electrodes and separator[78] were estimated in accordance with literature data.

Half-cell and full-cell measurements.—All investigated pouch-type cells and electrodes were supplied by the same manufacturer (CustomCells Itzehoe GmbH, Germany). CR2032-type coin cells were assembled in an argon filled glove box (M. Braun Inertgas-Systeme GmbH, Germany) containing graphite or NMC-111 electrode samples with a diameter of 14 mm and a metallic lithium electrode with a diameter of 15.6 mm (99.9% purity, 250 μm thickness, MTI Corporation, USA). To avoid electrical contact due to growth of lithium dendrites during operation, the two electrodes were separated by two glass fiber separators with a diameter of 16 mm (type 691 glass microfiber filter, 260 μm thickness each, VWR International, USA). Each coin cell was filled with 100 μL of electrolyte (Solvionic, France), containing 1 M lithium-hexaflourophosphate ($LiPF_6$) in ethylene carbonate (EC) : ethyl methyl carbonate (EMC) 3:7 (by weight). At least two coin cells were assembled for each electrode loading for both graphite and NMC-111. Following the formation procedure recommended by the manufacturer, the graphite and NMC-111 coin cells were charged and discharged at C/10 and C/5 for two cycles each followed by a final charge and discharge step at 1C between a lower and upper cutoff voltage of 0.1 V and 1.5 V (graphite) and 3.0 V and 4.3 V (NMC-111). The applied C-rate was chosen based on the estimated composite electrode loading (mg cm^{-2}) multiplied with the active material content (wt%) and specific capacity estimates (mAh g^{-1}) given by the manufacturer (see Table I).

The composite electrode loading was estimated by weighing both coated and uncoated/primed current collector samples prior to coin cell assembly. To determine the actual specific capacity of the active material, the coin cells were charged and discharged three times at C/50 between 0.01 V and 1.5 V (graphite) and 3.0 V and 4.2 V (NMC-111). The discharge capacity of the third C/50 cycle was considered to determine the specific capacity for each coin cell based on the estimated active material loading.

The mean values of all three electrode loadings shown in Table I are slightly higher than the manufacturer estimates which is well in line with previous studies.[11,79] Based on the measured specific capacities and the densities for both graphite and NMC-111 (see Table I), the maximum concentration $c_{s,\text{max}}$ (mol m^{-3}) can be determined. Assuming a complete utilization of the negative graphite electrode between 0.01 V and 1.5 V vs. Li/Li$^+$, $c_{s,\text{max,neg}}$ calculates as

$$c_{s,\text{max,neg}} = \frac{1}{F}\cdot 357.3\,\frac{\text{mAh}}{\text{g}}\cdot 3.6\,\frac{\text{As}}{\text{mAh}}\cdot 2.24\,\frac{\text{g}}{\text{cm}^3}\cdot 1\times 10^6\,\frac{\text{cm}^3}{\text{m}^3} = 29862\,\frac{\text{mol}}{\text{m}^3} \quad [14]$$

In case of the positive NMC-111 electrode, $c_{s,\text{max,pos}}$ needs to be estimated based on the molar mass M_{pos} of $LiNi_{1/3}Co_{1/3}Mn_{1/3}O_2$

$$c_{s,\text{max,pos}} = \frac{1}{M_{\text{pos}}}\cdot 4.75\,\frac{\text{g}}{\text{cm}^3}\cdot 1\times 10^6\,\frac{\text{cm}^3}{\text{m}^3} = 49242\,\frac{\text{mol}}{\text{m}^3} \quad [15]$$

Table I. Coin cell electrode composition, material and electrode characteristics.

Description	Unit	Negative electrode (neg) Graphite			Positive electrode (pos) NMC-111		
Electrode composition							
Active material content[s]	wt%		96			86	
Binder content[s]	wt%		2			6	
Conductive carbon content[s]	wt%		2			8	
Material characteristics							
Particle size (D50)[m]	µm		11			7	
Specific capacity[s]	mAh g^{-1}		350			145	
Specific capacity[m]	mAh g^{-1}		357.3			157.4	
Active material density[l]	g cm^{-3}		2.24[79]			4.75[96]	
Binder density[l]	g cm^{-3}		1.76[96]			1.76[96]	
Conductive carbon density[l]	g cm^{-3}		2.00[96]			2.00[96]	
		HP	BA	HE	HP	BA	HE
Electrode characteristics							
Coating thickness[m]	µm	28	63	102	47	74	150
Area specific capacity[s]	mAh cm^{-2}	1.1	2.2	3.9	1.0	2.0	3.5
Area specific capacity[m]	mAh cm^{-2}	1.19	2.44	3.84	1.11	2.24	3.90

[l]literature.
[m]measured.
[s]supplier information.

with

$$M_{\text{pos}} = \left(6.9410 + \frac{1}{3}\cdot 58.6934 + \frac{1}{3}\cdot 58.9332 + \right.$$
$$\left. + \frac{1}{3}\cdot 54.9380 + 2\cdot 16\right)\frac{\text{g}}{\text{mol}} = 96.46\,\frac{\text{g}}{\text{mol}} \qquad [16]$$

Assuming a complete lithiation of $LiNi_{1/3}Co_{1/3}Mn_{1/3}O_2$ at the lower cutoff voltage of the C/50 cycling procedure, the stoichiometry of the positive electrode can be calculated knowing its capacity. At the beginning of lithiation at 4.2 V vs. Li/Li$^+$, the stoichiometry y in $Li_yNi_{1/3}Co_{1/3}Mn_{1/3}O_2$ calculates as

$$y = 1 - \frac{M_{\text{pos}}}{F}\cdot 157.4\,\frac{\text{mAh}}{\text{g}}\cdot 3.6\,\frac{\text{As}}{\text{mAh}} = 0.433 \qquad [17]$$

based on the measured specific discharge capacity of 157.4 mAh g^{-1}. To further study the electrode balancing for the investigated single-layered pouch-type cells within the designated operating window, the NMC-111 coin cells were charged and discharged at C/50 between 2.5 V and 4.4 V for another two cycles.

Pouch-type cells with a HP, BA, and HE electrode loading were charged and discharged two times between 3.0 V and 4.2 V at C/50 whereas the applied C-rate was based on the measured discharge capacity of the cells derived from a constant current (CC) check up procedure at C/2, followed by a constant voltage (CV) phase at the upper and lower cutoff voltage of the cells until the current dropped below C/100. The last C/50 cycle was used for both coin cells and pouch-type cells in order to fit the measured half-cell potentials of the coin cells to the full-cell potentials of the pouch-type cells. As the electrodes used within the coin cells originate from a different batch as those incorporated in the pouch-type cells, a scaling of the half-cell data to the full-cell data was necessary during DVA for all electrode loadings. The DVA performed during full-cell charging (i.e. lithiation of the graphite anode and delithiation of the NMC-111 cathode) is shown in Fig. 2. As can be seen from the figure, the measured area specific capacities of the pouch-type cells slightly differ from the values declared by the manufacturer (i.e. 0.83, 1.85, and 3.65 mAh cm^{-2} vs. 1.0, 2.0, and 3.5 mAh cm^{-2}). Furthermore, the balancing between the electrodes shifts with increasing electrode loading. This becomes especially apparent when looking into the utilization window of the graphite anode (see Figs. 2a, 2c, and 2e) and when comparing the transition from LiC_{12} to LiC_6 (indicated by the peak at a lithiation degree of approximately 0.5 in the graphite anode in Figs. 2b, 2d, and 2f). The stoichiometry values for both graphite and NMC-111 derived from DVA are presented in Table II for all electrode loadings at cell voltages of 4.2 V (100% SoC), 4.15 V (96% SoC), and 3.0 V (0% SoC). For the BA loading, initial stoichiometries for cell voltages of 4.3 V (108% SoC), 4.0 V (82% SoC), and 3.85 V (67% SoC) were additionally derived to account for a varying initial SoC prior to the short circuit in accordance with experimental data.[12] Together with the thickness of the composite electrodes l_i measured at three different locations of the electrodes gained from post-mortem analysis,[12] the electrode composition and densities of the materials (see Table I), the electrode's porosity ϵ_l and active material volume fraction ϵ_s can be further estimated and is also shown in Table II. Based on the carried out C/50 half-cell measurements and the stoichiometry values derived from DVA, the equilibrium potential of both electrodes vs. Li/Li$^+$ was determined by averaging between lithiation and delithiation. The equilibrium potentials for both negative and positive electrode are shown in Figs. A1a and A1b in the appendix.

Literature-derived parameters.—In order to account for reversible heat effects, entropic coefficients were taken from Reynier et al.[70] and Lu et al.[71] for lithiated graphite and NMC-111, respectively (see Figs. A1c and A1d in the appendix). Fitting functions further used within this work are given in Eq. A8 and Eq. A9.

To present a simple model which is able to describe a cell's short circuit behavior without accounting for complex three-dimensional electrode structures,[80,81] the presented homogenized p2D model is parameterized based on one representative particle size within each electrode assuming a constant solid phase diffusion coefficient for each active material. This implies that both the impact of a particle size distribution[22,82–84] and the influence of solid phase diffusion coefficients which vary with Li-ion concentration[85] are neglected in the model. The influence of electrode morphology was considered in this work by scaling the electrolyte's inherent transport properties with the ratio between porosity ϵ_l and tortuosity τ of the electrodes and of the separator which is also known as the inverse MacMullin number N_M (see Table AI in the appendix). The tortuosity is estimated based on the porosity applying the commonly used Bruggeman relation[86] ($\tau = \epsilon^{-\alpha_B}$, see Table I). The range of the Bruggeman exponents α_B was chosen in accordance with previously published findings.[78]

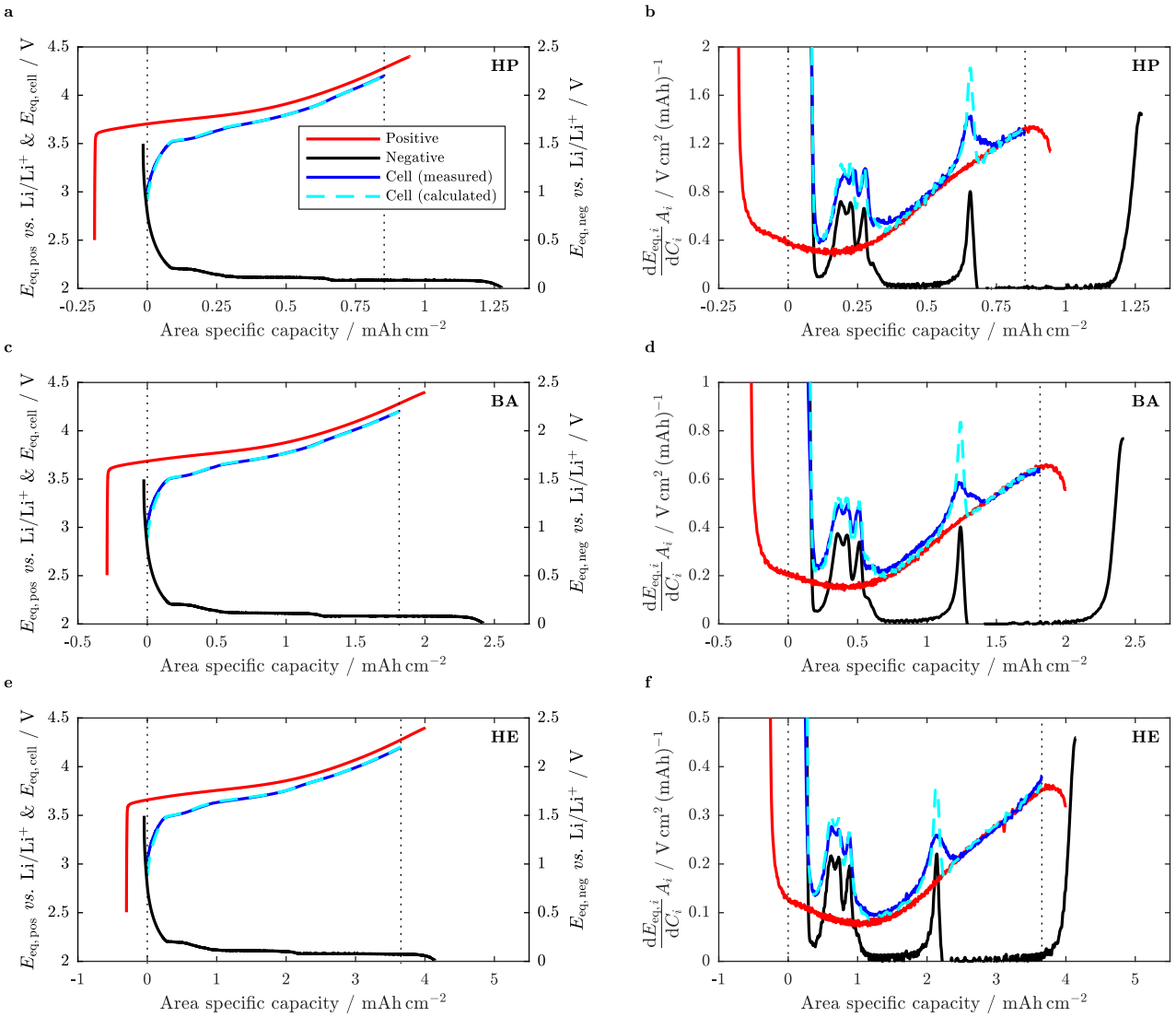

Figure 2. Derived electrode balancing for the HP (top: a and b), BA (middle: c and d), and HE (bottom: e and f) electrode loading based on the equilibrium voltage (left: a, c, and e) and differential voltage (right: b, d, and f) as a function of area specific capacity based on half-cell (graphite anode: lithiation, NMC-111 cathode: delithiation) and full-cell measurements (charge direction) at a constant current of C/50.

The fitted Bruggeman exponents vary between the three electrode loadings, which can be explained with uncertainties in porosity calculation and thickness measurements. Accounting for varying stoichiometries due to differing initial cell voltages and variations in electrode balancing (see Table II) as well as different temperatures, the solid phase diffusion coefficients were adapted allowing to fit the simulation data to experimental results (see Table III). The solid phase diffusion coefficients were chosen in accordance with reported data investigating the concentration dependency of Li-ion diffusion within both lithiated graphite[77,87,88] and NMC-111.[9,27] The plausibility of this approach is evaluated by implementing a concentration dependency of solid phase diffusion coefficients taken from literature[27,77] (see Figs. A1c and A1d in the appendix) as part of a sensitivity analysis at the end of the results section. Contrary to previous studies,[34,72] the reaction rate constants were considered independent from temperature as they showed almost no influence on the short circuit characteristics even when varied by up to one order of magnitude.

A mixture of 1 M $LiPF_6$ in ethylene carbonate (EC) : dimethyl carbonate (DMC) 1:1 (by weight) containing 2 wt% vinylene carbonate (VC) was used as electrolyte within the single-layered pouch-type cells.[12] With the electrolyte's transport properties depending on both salt concentration and temperature, literature data[34,73–76] is considered for describing the electrolyte's ionic conductivity κ_l (S m^{-1}), salt diffusion coefficient D_l (m^2 s^{-1}), cation transference number t_+ with respect to solvent, and thermodynamic factor TDF. To the knowledge of the authors, transport properties of electrolytes formed of $LiPF_6$ and organic solvents have not been studied so far at high concentrations (i.e. beyond 3.3 M[73]) or temperatures (i.e. beyond 60°C[73]). This can be best explained with the minor relevance of these conditions as long as a Li-ion cell is used within its designated operating window. As has been previously discussed, reported electrolyte properties are often presented as fitting functions following polynomial approximations which may cause problems if the electrolyte's transport properties are evaluated beyond the parameterization window.[8,81] This can result e.g. in an increasing ionic conductivity or diffusion coefficient at salt concentrations beyond the deflection point or the minimum of the polynomial fitting function, as shown in Figs. A2a and A2c in the appendix. To avoid this, fitting functions presented in literature are re-evaluated and amended for relevant concentration and temperature ranges (see Table AIII and Fig. A2 in the appendix). With the work of Valøen and Reimers[73] characterizing an EC:DMC based electrolyte with 10 vol% of polycarbonate (PC) from 7.7×10^{-6} M to 3.3 M $LiPF_6$ and from −10°C to 60°C, the simulation studies

Table II. Pouch-type cell material and electrode characteristics.

Description	Symbol	Unit	Negative electrode (neg) Graphite			Separator (sep) Polyolefin	Positive electrode (pos) NMC-111		
Material characteristics									
Equilibrium potential[m]	$E_{eq,\,i}$	V	see Fig. A1a			n/a	see Fig. A1b		
Anodic and cathodic reaction rate constant[l,72]	$k_{a/c,\,i}$	$m\,s^{-1}$	2×10^{-11}			n/a	2×10^{-11}		
Anodic and cathodic charge transfer coefficient[e]	$\alpha_{a/c,\,i}$	-	0.5			n/a	0.5		
Film resistance[l,34]	R_{film}	$\Omega\,m^{-2}$	0.0035			n/a	0		
Maximum solid phase concentration[c]	$c_{s,\,max,\,i}$	$mol\,m^{-3}$	29862			n/a	49242		
Solid phase eletronic conductivity[e]	$\sigma_{s,\,i}$	$S\,m^{-1}$	100			n/a	10		
Solid phase diffusion coefficient[e]	$D_{s,\,i}$	$m^2\,s^{-1}$	see Table III			n/a	see Table III		
Liquid phase ionic conductivity[l]	κ_l	$S\,m^{-1}$	Fitted function (see Table AIII and Figs. A2a and A2b)						
Liquid phase diffusion coefficient[l]	D_l	$m^2\,s^{-1}$	Fitted function (see Table AIII and Figs. A2c and A2d)						
Liquid phase transference number[l]	t_+	-	Fitted function (see Table AIII and Fig. A2e and A2f)						
Liquid phase thermodynamic factor[l]	TDF	-	Fitted function (see Table AIII and Figs. A2g and A2h)						
			HP	BA	HE		HP	BA	HE
Electrode characteristics									
Coating thickness[m]	l_i	µm	39	67	124	25	32	79	141
Porosity[c]	$\epsilon_{l,\,i}$	%	57.4	51.3	56.0	50	40.4	48.7	47.2
Active material volume fraction[c]	$\epsilon_{s,\,i}$	%	40.6	46.4	41.9	n/a	42.3	36.4	37.5
Tortuosity[e]	τ_i	-	$\epsilon_{l,\,neg}^{-2.7}$	$\epsilon_{l,\,neg}^{-1.8}$	$\epsilon_{l,\,neg}^{-1.5}$	$\epsilon_{l,\,sep}^{-1.8}$	$\epsilon_{l,\,pos}^{-1.7}$	$\epsilon_{l,\,pos}^{-1.1}$	$\epsilon_{l,\,pos}^{-0.8}$
Stoichiometry[c] at $E_{eq,\,cell}$ = 4.30 V / SoC = 108%			-	82.5	-		-	38.7	-
= 4.20 V = 100%			68.4	76.6	89.7		42.5	42.5	42.6
= 4.15 V = 96%	$\frac{c_s}{c_{s,\,max,\,i}}$	%	65.6	73.5	86.5		44.5	44.6	44.6
= 4.00 V = 82%			-	63.3	-		-	51.3	-
= 3.85 V = 67%			-	51.9	-		-	58.8	-
= 3.00 V = 0%			2.2	2.1	2.1	n/a	88.9	91.5	95.1

[c]calculated.
[e]estimated.
[l]literature.
[m]measured.

presented in this work are predominantly based on the reported findings.[73] Even though Mao et al.[34] have reported transport properties for an EC:DMC based electrolyte without the addition of PC as used within the pouch-type cells studied in this work, the origin and validity of these properties remains unclear. As part of a sensitivity analysis, the impact of the electrolyte's intrinsic transport properties on a cell's short circuit characteristics is studied at the end of this work for $LiPF_6$ in PC:EC:DMC,[73] EC:DMC,[34] EC:EMC,[74,75] and EC:DEC[76] (diethyl carbonate, DEC) based electrolytes.

The fully characterized (see Tables AI and AII in the appendix) and parameterized model (see Tables II and III as well as Table AIII in the appendix) was implemented in COMSOL Multiphysics 5.3a. Negative electrode, separator and positive electrode were discretized with 40, 40, and 80 nodes respectively as previously suggested.[34] The discretization in the positive electrode was chosen to be higher than in the negative electrode to be able to depict reported strong inhomogeneities in reaction and concentration.[34] The active material particles in both negative and positive electrode were discretized with an additional 20 nodes. Interpolation between the nodes was carried out following a cubic approach for all underlying variables. The applied discretization and interpolation schemes result in approximately 23500 degrees of freedom. With the chosen relative and absolute tolerance of 1×10^{-4}, the calculation takes approximately 15 min on a desktop computer (Intel Xeon E5-2687W 0 3.1 GHz with 64 GB RAM) until the current drops below C/100 which is considered the end of the short circuit procedure.

Table III. Fitted solid phase diffusion coefficients ($\times 10^{-14}\,m^2\,s^{-1}$) for both negative and positive electrode depending on stoichiometry, balancing, and temperature.

$D_{s,\,i}$ ($\times 10^{-14}\,m^2\,s^{-1}$)	Negative electrode (neg) Graphite			Positive electrode (pos) NMC-111		
	HP	BA	HE	HP	BA	HE
T = 25°C:						
initial $E_{eq,\,cell}$ = 4.30 V / SoC = 108%	-	8.0	-	-	0.2	-
= 4.15 V = 96%	8.0	8.0	8.0	0.55	0.25	0.15
= 4.00 V = 82%	-	8.0	-	-	0.3	-
= 3.85 V = 67%	-	8.0	-	-	0.4	-
T = 45°C:						
initial $E_{eq,\,cell}$ = 4.15 V / SoC = 96%	15.0	-	-	1.125	-	-
T = 55°C:						
initial $E_{eq,\,cell}$ = 4.15 V / SoC = 96%	20.0	-	-	1.5	-	-

Results and Discussion

Within this section, the presented modeling approach is validated first with respect to the predicted current and heat generation rate as a function of time and as a function of normalized discharged capacity. For this purpose, external short circuit conditions were simulated describing the behavior of single-layered pouch-type cells with varying electrode loadings (HP, BA, and HE) as well as at different cell temperatures (25°C, 45°C, and 55°C), initial cell voltages (4.30 V, 4.15 V, 4.00 V, and 3.85 V), and external short circuit resistances (0.0087 m Ω m^{-2}, 0.087 m Ω m^{-2}, and 1 m Ω m^{-2}) in accordance with experimental data presented in the first part of this combined work.[12] With the aid of the validated model, characteristics of external short circuits observed within both experiment and simulation are studied in more detail by evaluating the underlying mechanisms throughout the short circuit duration. These mechanisms are further evaluated by calculating each contribution to the overall cell polarization following the work of Nyman et al.[26] (see Table AII in the appendix). Based on these findings, a sensitivity study is presented, elaborating on the influence of transport properties and electrode morphology on a cell's short circuit characteristics.

Model validation.—In Fig. 3, model predictions (blue lines) are compared to previously reported measurement data (black lines) for all three electrode loadings at 25°C applying a 0 V short circuit condition (i.e. a first order Dirichlet boundary condition as presented in Table AI in the appendix). As can be seen from the figure, both the electrical (left: a, c, and e) and thermal behavior (right: b, d, and f) of all three electrode loadings can be reproduced very well with the model, not only as a function of short circuit duration t_{sc} (a to d) but also as a function of normalized discharged capacity ΔSoC (e and f). To determine C-rate (a and e), capacity related heat generation rate $\dot{Q}_{sc}/C_{4.2\,V}$ (W (Ah)$^{-1}$, b and f), ΔSoC (c, e, and f), and electrical energy related heat (d) in accordance with experimental data, the simulated current density (A m^{-2}), area specific heat rate (W m^{-2}), and area specific discharged capacity (Ah m^{-2}) are related to the cell's areal capacity $C_{4.2\,V}/A$ (Ah m^{-2}) between 4.2 V and 3.0 V (i.e. 0.83, 1.85, and 3.65 mAh cm^{-2} for the HP, BA, and HE loading as shown in Fig. 2).

When looking into Figs. 3a and 3e, the model is able to reliably follow the orders of magnitude in C-rate throughout the experimentally observed first and second plateau showing only minor discrepancies within the first few seconds of the short circuit or below 10% ΔSoC. As a shortcoming, the model is not able to describe the third plateau which was observed during experiments showing C-rates below 0.1 C beyond the fully discharged state (indicated via markers in Fig. 3). The experimentally observed over-discharge was previously attributed to a depletion of Li-ions within the electrolyte accompanied with a dissolution reaction of the anodic copper current collector allowing for an ongoing lithiation of the NMC-111 cathode even beyond complete depletion of the graphite anode. An additional side reaction describing the anodic copper dissolution process occurring beyond 3.1 V vs. Li/Li$^+$ was not implemented in the model which explains this discrepancy.

Adequately reproducing the experimentally observed similarity between the electrical and thermal behavior, the model correctly depicts the characteristic change in magnitudes of the capacity related heat generation rate throughout the first and second plateau (see Figs. 3b and 3f). However, a distinct delay between the measured and predicted heat generation rate can be observed. As previously described,[12] the chosen test setup showed a constant time delay of 21 s between calorimetric and potentiostatic data. This time delay can be explained with the thermal inertia of the used copper blocks increasing the heat capacity of the system to guarantee quasi-isothermal test conditions when determining the generated heat based on a transient temperature increment (ΔT<1°C). The reported time delay can be confirmed when comparing the model predictions with the measurement data (see Figs. 3b and 3d). The calculated heat generation rate which is primarily based on the simulated cell current density and calculated total overpotential throughout the electrodes as well as the voltage drop across the separator (see Eq. A5 to Eq. A7 in the appendix), shows a slightly higher deviation from the calorimetric measurements than the difference between the calculated C-rate and the potentiostatic measurements (see Figs. 3e and 3f). Based on the calculated adiabatic temperature increase as presented in the first part of this combined work, an integration error seems to occur in calculating the generated heat and, therefore, the calculation of heat generation rate. This integration error is ranging between 9% and 12% for the three electrode loadings (compare black and gray lines in Fig. 3d) which would also explain the previously discussed difference in the calculated effective overvoltage of the cells ranging between 3.3 V (HE) and 3.4 V (HP) compared to the nominal cell voltage of 3.7 V.[12]

It worth emphasizing here that the presented model is capable to qualitatively and quantitatively describe a cell's behavior during high currents without applying complex three-dimensional electrode models and without implementing extensions to the original Newman-type model such as a particle size distribution or a concentration dependency of solid phase transport parameters. This, however, is only the case provided that the only reaction that is occurring is a de-/intercalation reaction of Li-ions within the anodic and cathodic host lattice without any further side reactions which might be triggered at elevated temperatures. This implies that by solely depicting overall morphology and balancing related characteristics of the electrodes such as active material volume fraction, porosity, tortuosity, and stoichiometry, the homogenized model is able to describe the effect of electrode loading on the cell's short circuit characteristics, resulting in an increase in C-rate and capacity related heat generation rate with lower electrode loadings.

By further accounting for temperature dependent electrolyte transport properties according to Valøen and Reimers[73] (see Table AIII and Fig. A2 in the appendix), temperature dependent diffusion coefficients of the active materials (see Table III) and the temperature dependency of Butler-Volmer reaction kinetics (see Eq. 12 and Eq. 13 as well as Table AI in the appendix), the experimentally observed effect of temperature on the cell's short circuit behavior can be also described (see Fig. 4). Furthermore, a limited increase in C-rate and capacity related heat generation rate (not shown here) at temperatures beyond 45°C especially throughout the second plateau can be confirmed.

By accounting for a variation in stoichiometry within the active material particles (see Table II) and by considering varying solid phase diffusion coefficients (see Table III), the influence of initial cell voltage or SoC on the cell's short circuit behavior can be further evaluated (see Fig. 5). Confirming experimental results, the first plateau and the beginning of the second plateau are almost unaffected by the initial cell voltage or SoC whilst the duration of the short circuit scales with the discharged capacity.

By altering the boundary conditions at the positive terminal (see second order Neumann boundary condition in Table AI in the appendix), also the impact of varying external short circuit resistances can be analyzed in terms of C-rate, ΔSoC, and cell voltage (see Fig. 6).

Remaining deficiencies of the model especially within the first plateau can be reduced by adapting the model as discussed. This is exemplary shown for concentration dependent solid phase diffusion coefficients at the end of the results section as part of a sensitivity analysis. However, the accuracy of the presented model is satisfying, keeping in mind that a standard p2D model is used, which is only modified by accounting for a diffusion limited Butler-Volmer equation.

Rate limiting mechanisms.—With the presented model being capable of describing the experimentally observed characteristic change in magnitudes of both C-rate and capacity related heat generation rate, the model and the chosen set of parameters are considered to further identify and analyze the underlying mechanisms resulting in the observed cell behavior.

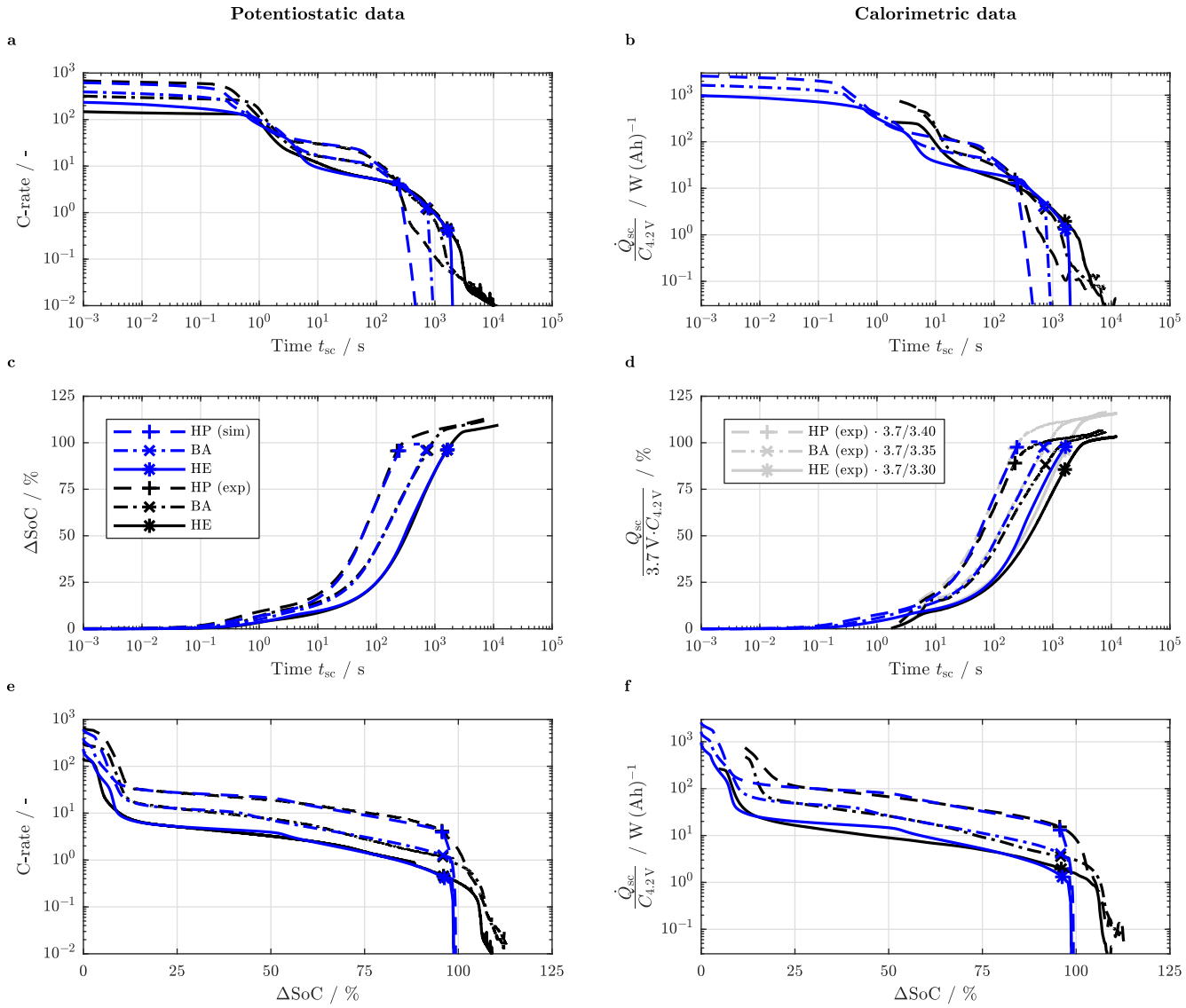

Figure 3. Comparison of measured (black lines and markers) and predicted (blue lines and markers) electrical (left: a, c, and e) and thermal cell behavior (right: b, d, and f) during a 0 V short circuit event for the HP (dashed lines), BA (dash-dotted lines), and HE loading (solid lines) at 25°C and an initial cell voltage of 4.15 V as a function of short circuit duration t_{sc} (a to d) and as a function of normalized discharged capacity ΔSoC (e and f) for the C-rate (a and e), capacity related heat generation rate (b and f), ΔSoC (c), and electrical energy related heat (d). The gray lines and markers in d represent qualitatively corrected measurement data. Markers indicate 0% SoC.

Evolution of Li-ion concentration distribution.—As rate limitation is generally regarded to be caused by a premature saturation or depletion of Li-ions in the solid and liquid components of a cell, the spatial Li-ion concentration throughout the electrodes and separator is studied at distinct times of the short circuit duration.

For this purpose, the BA loading with an initial cell voltage of 4.15 V or 96% SoC exposed to a 0 V short circuit condition at a temperature of 25°C is taken as a reference. From Fig. 3 and Fig. 5, three mentioned plateaus can be clearly identified: around 300 C in the beginning of the short circuit (below 1 s), around 10 C to 20 C with ongoing discharge (10 s to 100 s) and below 0.1 C at the end of the short circuit (1000 s to 10000 s). Neglecting an additional copper dissolution reaction within the anode, the observations made here focus on the first two plateaus and transition phases around 1 s to 10 s for the first plateau changing into the second and around 100 s to 1000 s for the second plateau passing into the third. When looking into the Li-ion concentration (see Fig. 7) in the liquid (left: a, c, e, and g) and in the solid components of the cell (right: b, d, f, and h) up to 0.32 s (a and b), between 0.5 s and 8 s (c and d), between 20 s to 160 s (e and f), and from 200 s to 800 s (g and h), characteristic concentration profiles for each plateau and transition phase can be observed in both the negative and positive electrode.

Throughout the first plateau (see Figs. 7a and 7b), the cell is discharged without major limitations in mass transport. Within the positive electrode, the salt concentration decreases forming a minimum near the separator whilst the Li-ion concentration at the surface of the active material particles increases forming a maximum at the boundary between the separator and electrode domain. Within the negative electrode, the salt concentration increases forming a maximum near the separator whilst the surface concentration of the active material particles decreases with the lowest concentration at the boundary between separator and electrode. However, the surface concentration varies in a slower fashion as a function of time compared to the positive electrode due to the larger diffusion coefficient of graphite (see Table III). The observed inhomogeneous Li-ion concentration is fundamentally based on a strongly non-uniform reaction across the electrodes with a larger pore-wall flux at the separator interface (not shown here). For the chosen set of parameters, the surface concentration approaches

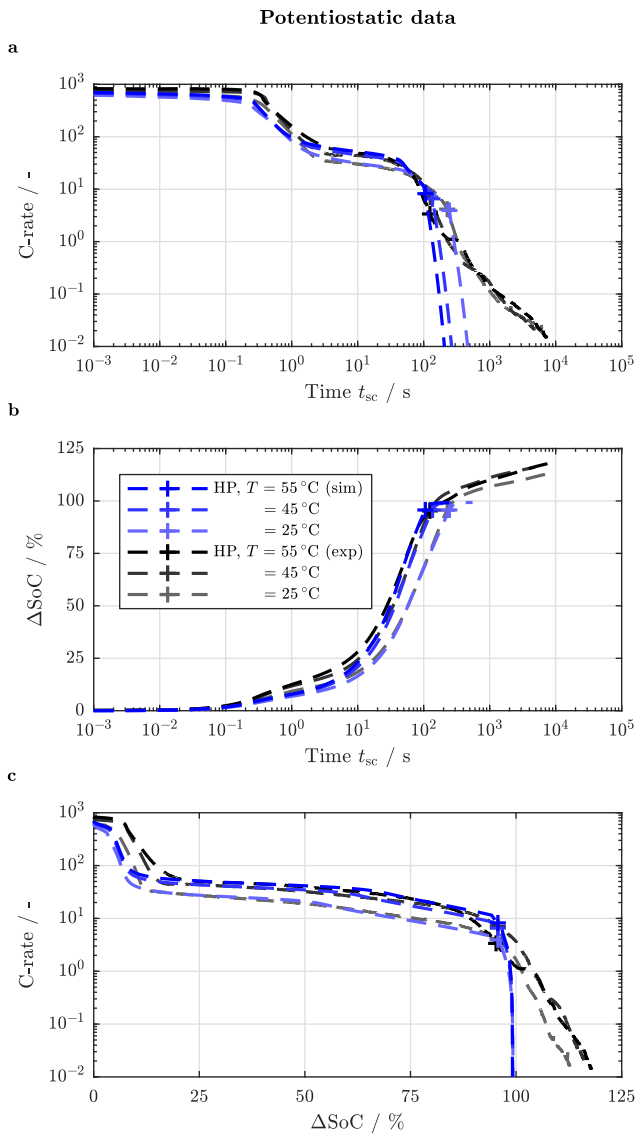

Figure 4. Comparison of measured (black lines and markers) and predicted (blue lines and markers) electrical cell behavior during a 0 V short circuit event for the HP loading at an initial cell voltage of 4.15 V and temperatures of 55°C, 45°C, and 25°C as a function of short circuit duration t_{sc} (a and b) and as a function of normalized discharged capacity ΔSoC (c) for the C-rate (a and c) and ΔSoC (b). Markers indicate 0% SoC.

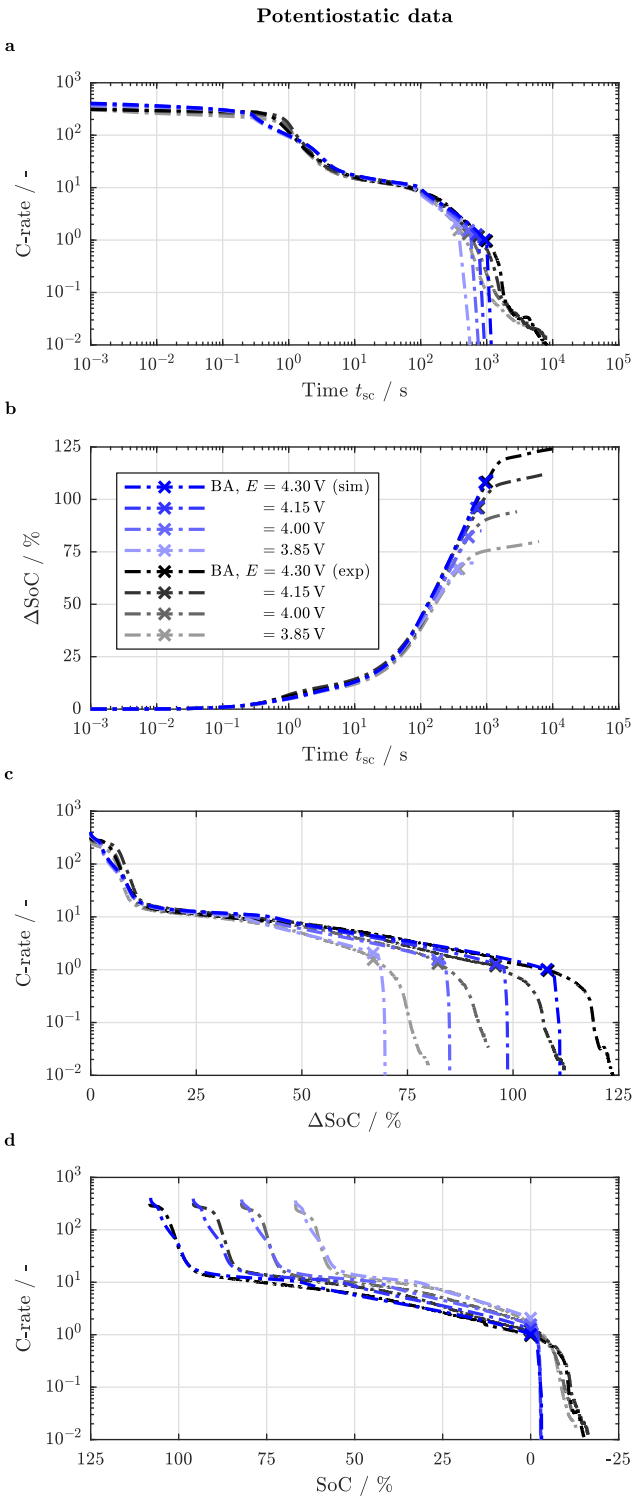

Figure 5. Comparison of measured (black lines and markers) and predicted (blue lines and markers) electrical cell behavior during a 0 V short circuit event for the BA loading at 25°C and initial cell voltages of 4.3 V, 4.15 V, 4.0 V, and 3.85 V as a function of short circuit duration t_{sc} (a and b), as a function of normalized discharged capacity ΔSoC (c), and as a function of SoC (d) for the C-rate (a, c, and d) and ΔSoC (b). Markers indicate 0% SoC.

the fully lithiated state throughout the entire positive electrode at the end of the first plateau, which results in large reaction and mass transport based overpotentials. As a result, the current and consequently also the heat generation rate drop toward the second plateau. During the observed transition period between the plateaus (see Figs. 7c and 7d), the salt concentration within the positive electrode approaches the fully depleted state with the minimum concentration forming at the current collector interface which allows the surface concentration within the positive electrode to decrease again based on the reduced pore-wall flux in this area and a simultaneously occurring homogenization of concentration gradients within the active material particles. Similarly, the surface concentration within the negative electrode slightly increases throughout the electrode whilst the maximum salt concentration moves from the separator to the current collector at concentrations exceeding 2 M (i.e. 2 mol L^{-1}). During the second plateau (see Figs. 7e and 7f), the minimum salt concentration is still located at the current collector interface and the maximum solid phase concentration is still located at the separator interface of the positive electrode. Whilst the region which is affected by a depletion in salt concentration is shrinking toward the current collector, the area which is affected by a saturation of the active material particles is growing from the separator toward the current collector until the active material particles are fully saturated at the surface within the entire

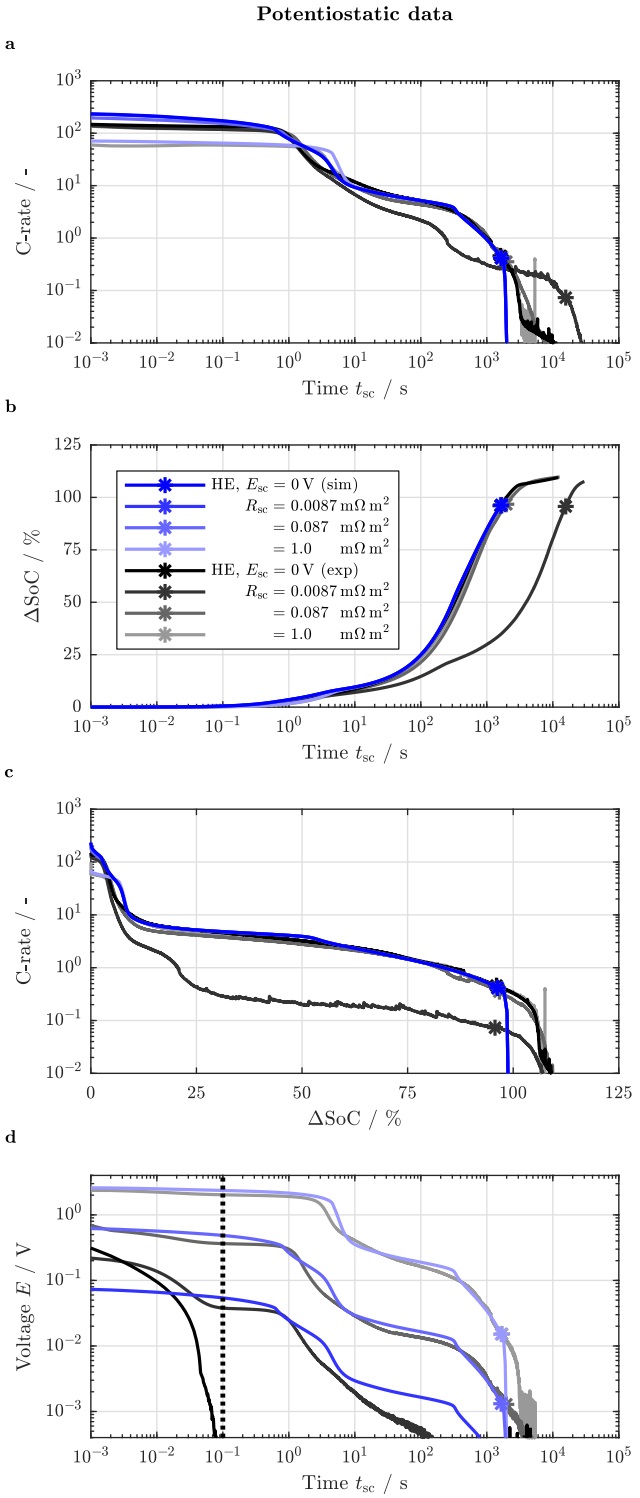

Figure 6. Comparison of measured (black lines and markers) and predicted (blue lines and markers) electrical cell behavior during a 0 V short circuit event and external short circuit resistances of 0.0087 mΩm^2, 0.087 mΩm^2, and 1 mΩm^2 for the HE loading at 25°C and an initial cell voltage of 4.15 V as a function of short circuit duration t_{sc} (a, b, and d) and as a function of normalized discharged capacity ΔSoC (c) for the C-rate (a and c), ΔSoC (b), and cell voltage (d). The vertical dotted line in d indicates the duration (100 ms) until a stable regulation of the used potentiostat was achieved. Markers indicate 0% SoC. The cell that was exposed to 0.0087 mΩm^2 during experiments showed an abnormal, high resistance behavior.

positive electrode. The reduced current density occurring throughout the second plateau allows for a homogenization in salt concentration throughout the electrodes. Despite the saturated surface concentration within the positive electrode, the ongoing discharge process results in a decreasing surface concentration within the negative electrode approaching the fully depleted state. This process is dominating the transition from the second plateau to the third plateau (see Figs. 7g and 7h), resulting in a strongly decreasing current and heat generation rate. At the end of the simulation of the short circuit, the surface concentration is completely depleted throughout the negative electrode resulting in a slightly decreasing surface concentration within the positive electrode whilst the comparably low cell currents allow for an ongoing homogenization in salt concentration approaching the initial concentration of 1 M (dashed line in Fig. 7g).

At the very end of the short circuit, the simulated potential at the boundary between current collector and negative electrode increases beyond 3.1 V[89] vs. Li/Li$^+$ (see Fig. 8) which supports the previously stated assumption of an ongoing intercalation reaction within the positive electrode based on an anodic copper dissolution reaction and salt depletion throughout the third plateau.[12]

Breakdown of cell polarization.—From the above, the transients in magnitudes of current and heat generation rate can be explained based on the salt and surface concentration at the boundaries of the positive electrode and the surface concentration at the boundaries of the negative electrode. Together with the resulting calculated polarization within the electrodes and the voltage drop across the separator as presented in Table AII in the appendix, a thorough evaluation of the observed short circuit behavior can be carried out.

This is exemplarily shown in Fig. 9 for the BA loading both as a function of short circuit duration t_{sc} (left: a, c, and e) and as a function of normalized discharged capacity ΔSoC (right: b, d, and f). When looking into the validation (top: a and b), the aforementioned three plateaus (I, II, and III) as well as the transition phases between the plateaus (I-II and II-III) can be identified. Plateau II can be further subdivided into two parts (IIa and IIb) based on a distinctly varying slope of the plateau which can be observed in both representations. Each phase shows different dominating voltage losses (middle: c and d) which can be correlated to the Li-ion concentration at the surface of the solid active material particles and to the average salt concentration in the liquid electrolyte at the boundaries of the electrodes (bottom: e and f). Within the first plateau, ohmic losses (Ω) within the liquid electrolyte throughout both electrodes and separator as well as Butler-Volmer (BV) reaction kinetics within the negative electrode (see Figs. 9c and 9d) are dominating the cell polarization. Even though the largest currents can be observed for the first plateau, ohmic losses within the solid phase range below 15 mΩ which is why they are not explicitly shown in the legend of Figs. 9c and 9d. The larger contribution of Butler-Volmer reaction kinetics within the negative electrode compared to the positive electrode can be explained with the additionally considered film resistance resulting in an increased voltage drop across the solid electrolyte interphase (see Table II and Table AI in the appendix), the negative electrode's approximately 30% smaller reaction surface area based on particle size, electrode thickness, and active material volume fraction as well as the 40% smaller exchange current density based on the balancing-related stoichiometry within the active materials (see Table I, Table II, and Table AI). Approaching the transition phase I-II, the polarization based on solid phase diffusion (D) within the active material particles of the positive electrode is substantially increasing. Due to the predicted premature saturation of the surface concentration throughout the entire positive electrode, the simulated transition phase I-II begins slightly earlier than observed during the measurements (see Figs. 9a and 9e), as also apparent in the ΔSoC based representation (see Figs. 9b and 9f). As soon as the minimum salt concentration is located at the current collector boundary of the positive electrode, the over-predicted limitation decreases and the simulation data again follows the measurement data very well. Due to the mass transport based limitation of the reaction within the positive electrode, the reaction overpotential increases considerably

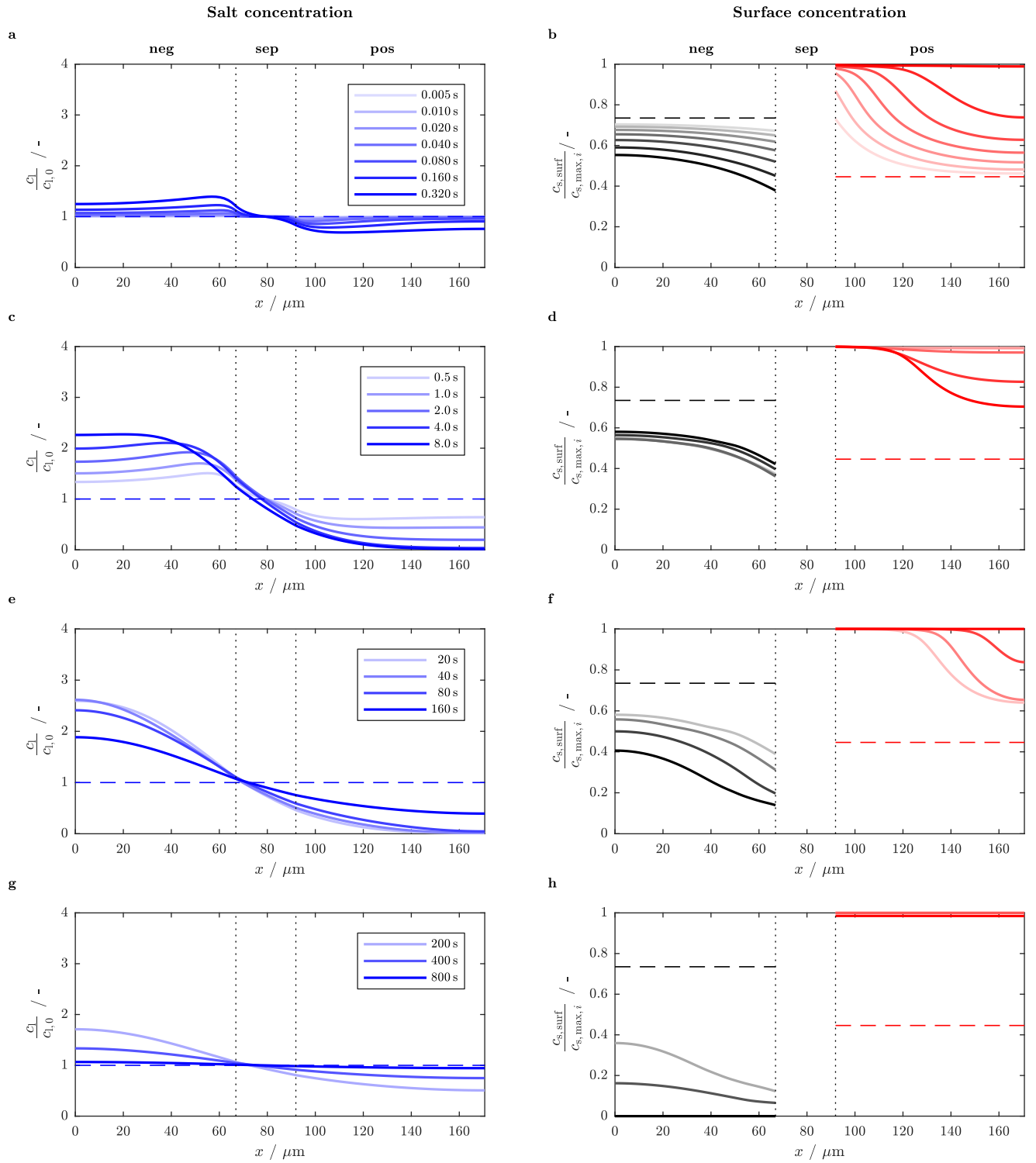

Figure 7. Predicted spatial distribution of normalized salt concentration within the liquid phase (left: a, c, e, and g) and normalized surface concentration within the solid phase (right: b, d, f, and h) during a 0 V short circuit event for the BA loading at 25°C and an initial cell voltage of 4.15 V during the first plateau (a and b) and the approach toward the second plateau (c and d) as well as throughout the beginning of the second plateau (e and f) and the end of the second plateau approaching the third plateau (g and h).

whilst the current drops and, hence, the ohmic based voltage drop decreases throughout the electrodes and separator following the current. After plateau I and the transition phase I-II consuming about 10% of the cell's capacity within less than 5 s, the reaction overpotential within the positive electrode remains dominating (ca. 3 V) throughout the first part of the second plateau (IIa) which forms due to a simultaneously occurring saturation of the active material particles near the separator and salt depletion near the current collector (see Figs. 7e and 7f as well as Figs. 9e and 9f). The occurring large liquid phase concentration gradients throughout the electrodes and separator as well as the salt concentration approaching depletion within the positive electrode result in an increasing diffusion based polarization within the liquid phase (dashed black, blue, and red lines in Figs. 9c and 9d). Similar to the total ohmic contribution of the solid phase,

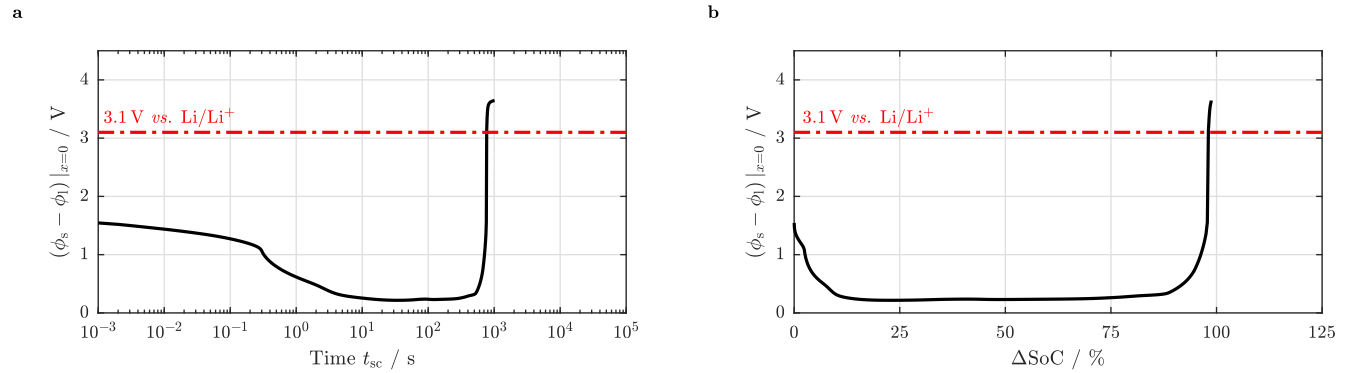

Figure 8. Simulated potential vs. Li/Li$^+$ of the negative electrode at the current collector interface ($x = 0$) as a function of short circuit duration t_{sc} (a) and as a function of normalized discharged capacity ΔSoC (b) indicating the likeliness of an anodic copper dissolution reaction[89] at the very end of the short circuit event with potentials exceeding 3.1 V vs. Li/Li$^+$.

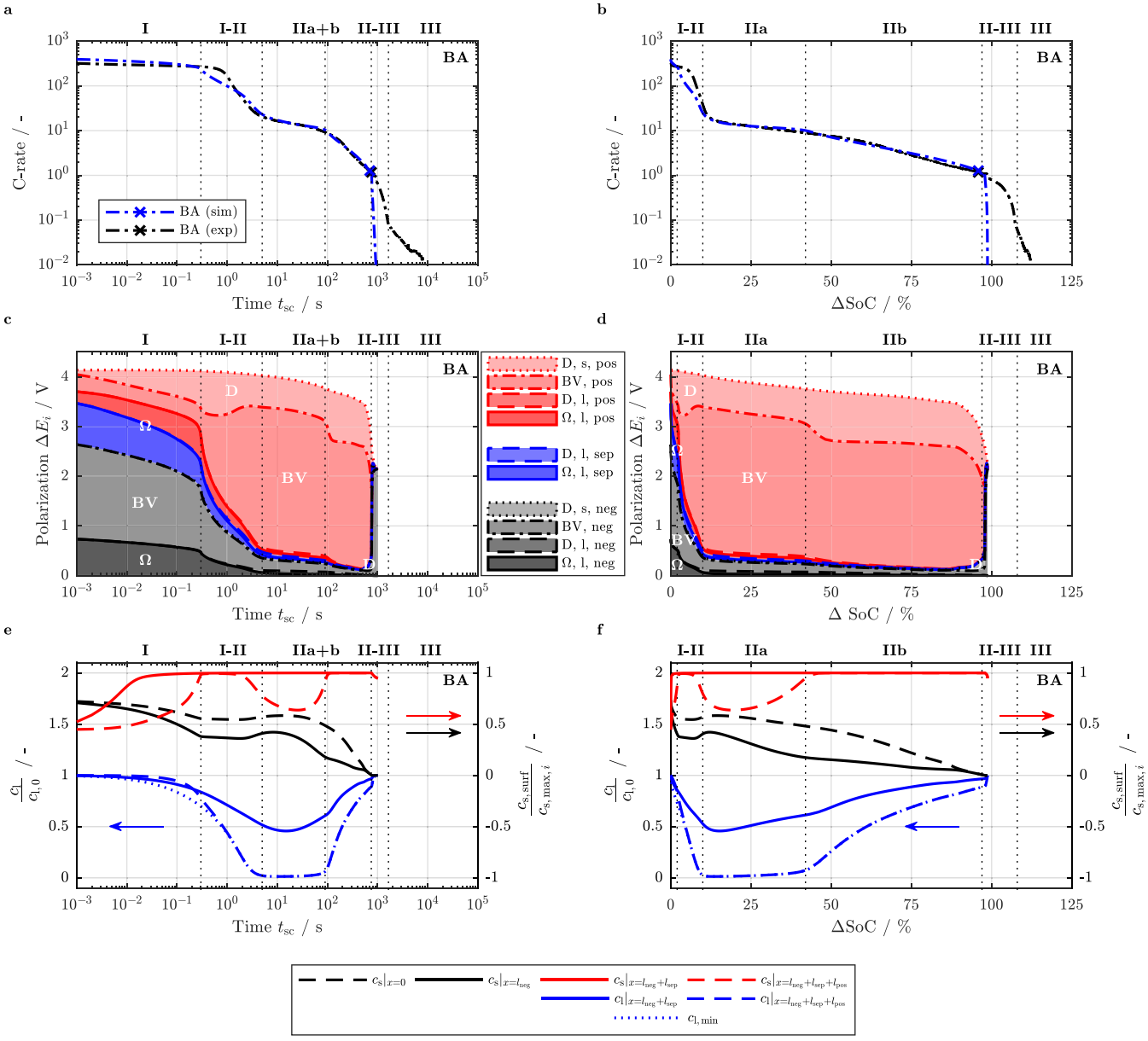

Figure 9. Measured and predicted phases of a short circuit during a 0 V short circuit event for the BA loading at 25°C and an initial cell voltage of 4.15 V observed in C-rate (top: a and b), the corresponding predicted polarization throughout the electrodes and separator (middle: c and d) resulting from the underlying normalized solid (surface) and liquid phase concentration (average) at distinct locations of the cell (bottom: e and f) as a function of short circuit duration (left: a, c, and e) and as a function of normalized discharged capacity (right: b, d, and f).

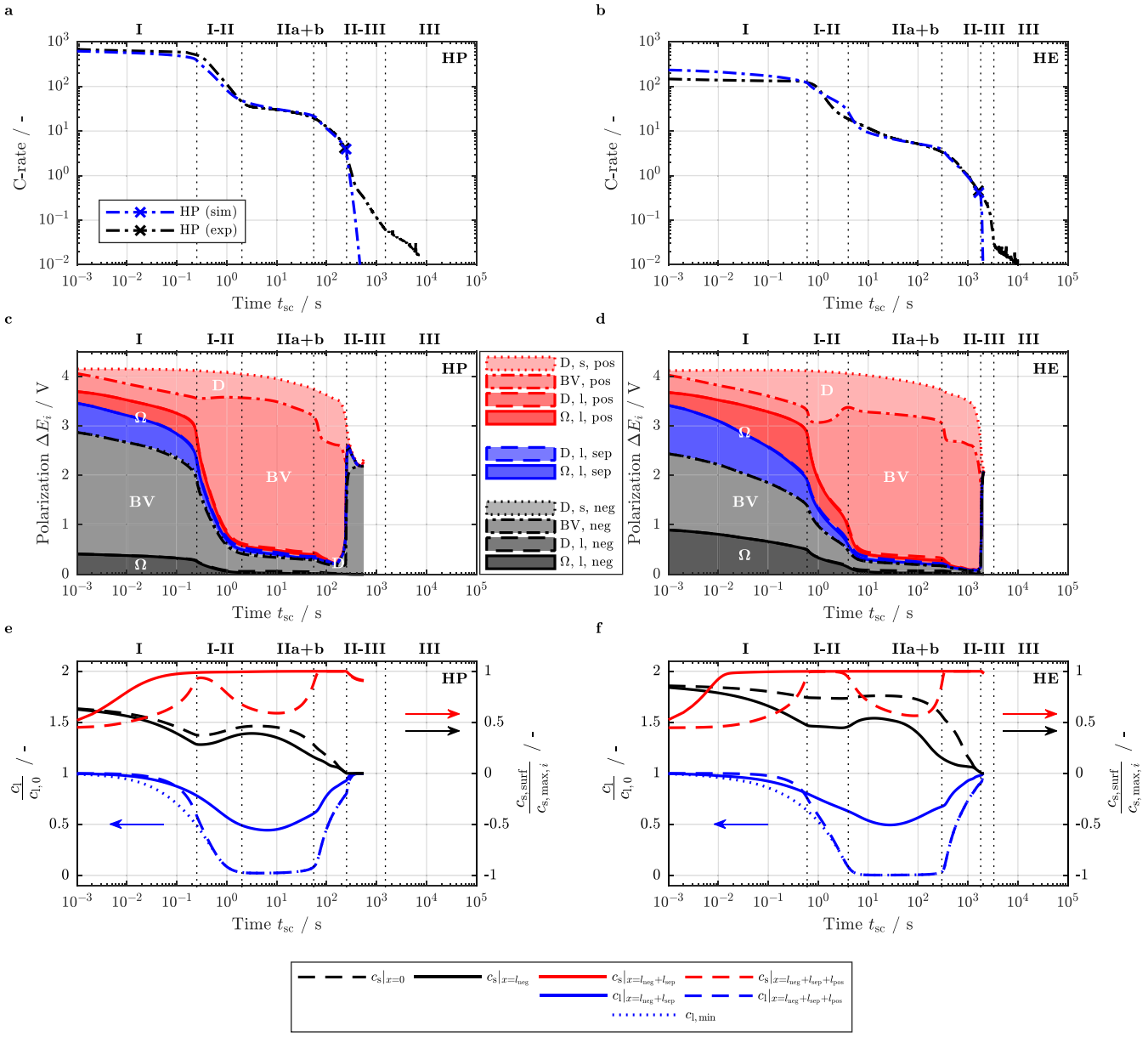

Figure 10. Measured and predicted phases of a short circuit during a 0 V short circuit event for the HP (left: a, c, and e) and HE loading (right: b, d, and f) at 25°C and an initial cell voltage of 4.15 V observed in C-rate (top: a and b), the corresponding predicted polarization throughout the electrodes and separator (middle: c and d) resulting from the underlying normalized solid (surface) and liquid phase concentration (average) at distinct locations of the cell (bottom: e and f) as a function of short circuit duration.

this polarization only plays a minor role during the entire short circuit (150 mΩ at its maximum in plateau II). After the first part (IIa) of the second plateau consuming another 32% of the cell's capacity within 85 s, the second part (IIb) is characterized by a fully saturated surface concentration within the entire positive electrode (see Figs. 9e and 9f). This change of dominating mass transport limitations is not only reflected in the slope of plateau IIa and IIb in Figs. 9a and 9b but also in the contribution of the positive electrode's solid phase diffusion to the observed cell polarization (ca. 1 V). Independent of the characteristics of mass transport limitation within the positive electrode (i.e. a combination of solid and liquid phase in IIa vs. solid phase alone in IIb), the reaction overpotential remains dominating. At the end of plateau IIb consuming 55% of the cell's capacity within 640 s, the mass transport within the solid phase and the reaction overpotential within the negative electrode become dominant due to the depleted surface concentration of the active material particles. With simulated anode potentials exceeding 3.1 V vs. Li/Li$^+$ at the negative electrode's current collector (see Fig. 8), the transition phase II-III is likely to be characterized by an ongoing Li-ion intercalation reaction within the positive electrode driven by the continuing de-intercalation reaction of the negative electrode and a simultaneously occurring anodic copper dissolution reaction until the positive electrode is completely lithiated throughout plateau III.

Influencing factors on cell polarization.—When comparing the HP and HE electrode loading to the BA loading as function of short circuit duration t_{sc} (see Fig. 10 and Fig. 9 on the left), the variations between the three loadings can be correlated to differences in the polarization behavior. The larger C-rate of the HP loading is primarily based on lower ohmic losses within the liquid electrolyte based on the reduced electrode thickness and the resulting smaller concentration gradients throughout the electrodes and separator. The more homogeneous electrode utilization further reduces the solid phase diffusion based polarization especially in the positive electrode of the HP loading. Based

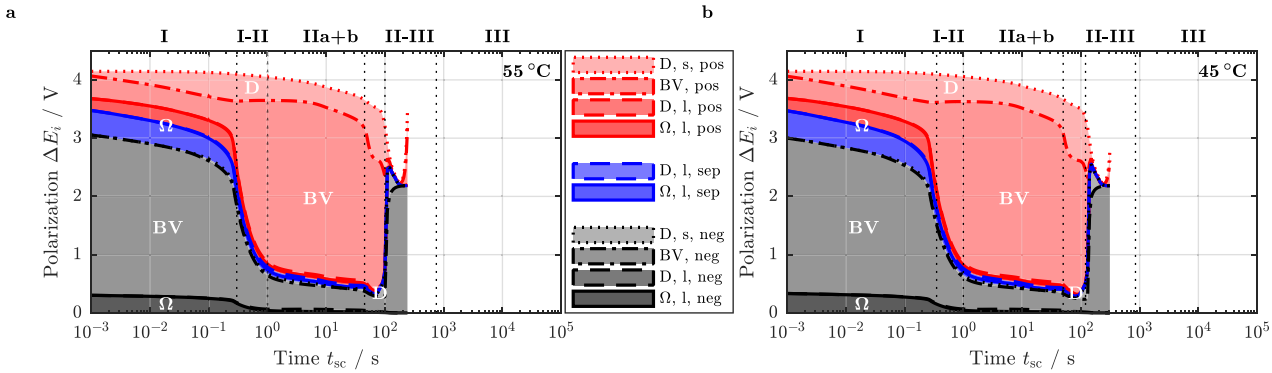

Figure 11. Predicted polarization during a 0 V short circuit event at an initial cell voltage of 4.15 V throughout the electrodes and separator for the HP loading at 55°C (a) and at 45°C (b) as a function of short circuit duration.

on the reduced electrode loading and, hence, smaller reaction surface area together with a reduced initial Li-ion concentration within the negative electrode due to the varied electrode balancing (see Table II), the reaction overpotential especially within the first plateau is considerably increased compared to the BA and HE loading. As a result of the logarithmic representation, the observed mass transport limitation of reaction kinetics within the negative electrode at the end of the short circuit becomes more pronounced at earlier times. Interestingly, the predicted transient change from plateau I to II can be described very well for the HP loading compared to the BA and HE loading based on a lacking occurrence of a solid phase diffusion limitation within the positive electrode during the transition phase I-II. Extensive simulation studies carried out as part of this work have shown that the solid phase diffusion coefficient within the positive electrode defines the initiation and the slope of plateau IIb which consumes the largest amount of charge throughout the short circuit. However, a larger diffusion coefficient would be beneficial to describe the transition phase I-II adequately for the BA and HE loading, avoiding a solid phase diffusion limitation within the transition phase. As the first plateau and the first transition phase only account for less than 10% of the cell's capacity, the focus of parameterization was laid on plateau IIb. This will be discussed in more detail as part of a sensitivity analysis.

When comparing the polarization of the HP loading at 55°C to 45°C (see Figs. 11a and 11b) and 25°C (see Fig. 10c), the experimentally observed limited impact of the cell's temperature beyond 45°C can be explained. An increase from 25°C to 45°C considerably reduces the ohmic losses within the liquid electrolyte based on an enhanced ionic conductivity (see Table AIII and Fig. A2 in the appendix) allowing for a larger charge transfer overpotential and consequently an increased pore-wall flux. This effect is further enhanced due to the reduced solid phase diffusion polarization based on the fitted temperature dependency of the solid phase diffusion coefficients.[34,72] Beyond 45°C, a marginal variation in the occurring polarization contributions can be observed, supporting the previously stated limited impact of temperature on the dynamics of the short circuit based on mass and charge transport.[12]

In Fig. 12, the influence of initial cell voltage or SoC on the occurring cell polarization is shown. The experimentally observed similarity between cells with varying initial cell voltage or SoC throughout phases I, I-II, and IIa, can be confirmed as the contribution of each mechanism to the entire cell polarization is fairly similar between 4.30 V (108% SoC) and 3.85 V (67% SoC). Despite the reduced overall polarization based on the lower cell voltage, especially the solid phase diffusion based polarization within the positive electrode is reduced due to higher initial concentrations and consequently reduced concentration gradients throughout the short circuit duration. Furthermore, the initial cell current is slightly lower for lower cell voltages, reducing ohmic losses within the liquid electrolyte. Due to the lower cell capacity, plateau IIb is considerably reduced approaching the transition phase II-III at earlier times.

With increasing external short circuit resistance, plateau I and the transition phase I-II are considerably affected (compare Fig. 13 to Fig. 10d) whereas plateau IIa and especially IIb are almost not influenced. This implies that as long as the short circuit resistance is small enough so that liquid phase depletion and solid phase saturation occur within the positive electrode, the second plateau will show the same characteristic shape.

To sum up, the presented standard p2D-model is able to shed light on the dominating mechanisms resulting in the experimentally observed characteristics occurring during quasi-isothermal external short circuit tests. The model based evaluation reveals that the first and second plateau as well as the transition phases between the two and the approach toward the third plateau are dominated by reaction kinetics within the negative electrode (I and II-III) as well was reaction kinetics within the positive electrode (I-II, IIa, and IIb). With the largest currents occurring within the first plateau, ohmic resistances

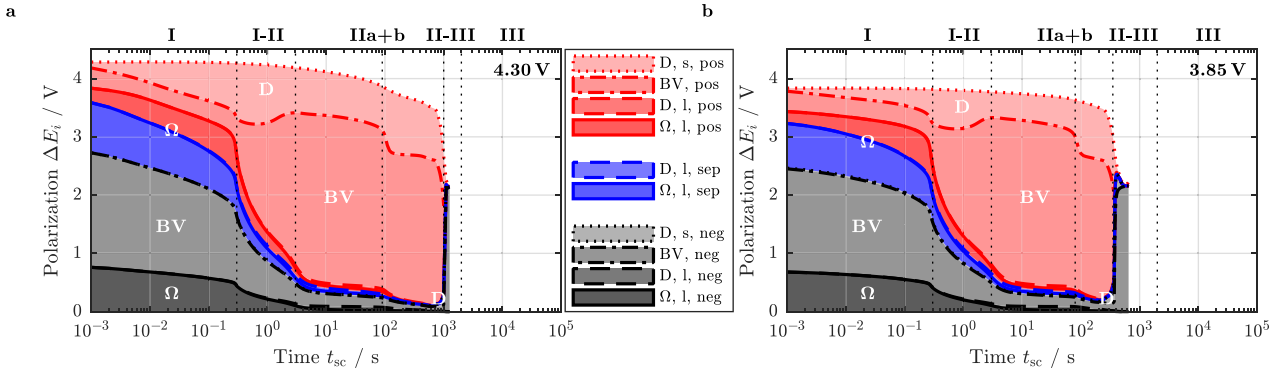

Figure 12. Predicted polarization during a 0 V short circuit event at initial cell voltages of 4.3 V (a) and 3.85 V (b) throughout the electrodes and separator for the BA loading at 25°C as a function of short circuit duration.

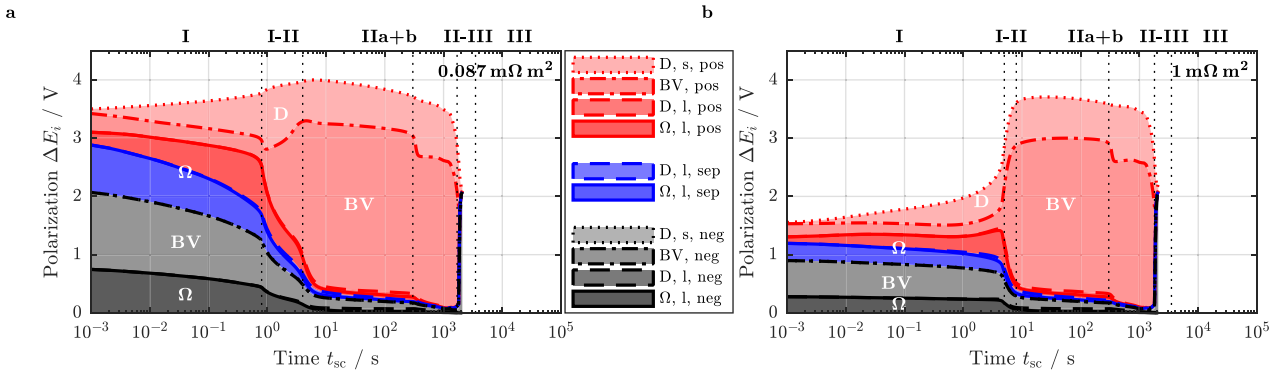

Figure 13. Predicted polarization during 0.087 mΩm^2 (a) and 1 mΩm^2 (b) external short circuit events at an initial cell voltage of 4.15 V and 25°C for the HE loading as a function of short circuit duration.

within the liquid electrolyte are forming a major contribution whilst solid phase diffusion polarization is becoming more important with ongoing duration of the short circuit. The characteristic second plateau with its two stages IIa and IIb is dominated by mass transport limited reaction kinetics throughout the entire positive electrode based on a combination of liquid phase depletion and solid phase saturation (IIa) as well as an exclusive solid phase limitation (IIb). Independent of the electrode loadings, cell temperatures, cell voltages, and external short resistances studied in this investigation, the sequence of rate limitation remains the same throughout the external short circuits. However, the contribution of each underlying mechanism based on the Li-ion concentration distribution throughout the electrodes and separator is varying for the investigated cells and applied short circuit conditions.

Sensitivity analysis.—As discussed within the model validation part and the analysis of rate limiting mechanisms, some discrepancies remain between the predicted and experimentally observed short circuit behavior for the chosen set of parameters, especially at early times combined with increasing electrode loadings. For this purpose, a sensitivity analysis is carried out for various transport parameters that have been reported in literature, accounting for a concentration dependency within both solid and liquid phase. In the second part of this sensitivity analysis, the influence of electrode characteristics defining the suitability of a cell toward high power or high energy applications is studied in terms of short circuit dynamics.

Influence of concentration dependent transport properties.—Only little work has been presented so far dealing with a concentration dependency of Li-ion diffusion coefficients within the active materials. Previous findings of Levi and Aurbach[77] and Markevich et al.[87] describing a considerable concentration dependency of the Li-ion diffusion coefficient within lithiated graphite have been recently confirmed by Malifarge et al.[88] The concentration dependency of Li-ion diffusion coefficients in NMC electrodes has been studied for varying compositions by Noh et al.[9] and explicitly for NMC-111 by Wu et al.[27] The experimental data supplied by Levi and Aurbach[77] and Wu et al.[27] as shown in Figs. A1e and A1f was fitted according to Eq. A10 and Eq. A11 in the appendix which is further used here. As can be seen from Figs. 14a and 14b, accounting for a concentration dependency of solid phase diffusion coefficients improves the prediction accuracy at the beginning of the short circuit, especially throughout transition phase I-II (compare Figs. 14a and 14b to Figs. 9a and 9b). This can be explained by the increased diffusion coefficient of NMC-111 (ca. 3.0×10^{-14} m^2 s^{-1} vs. the effective value of 0.25×10^{-14} m^2 s^{-1}) and the reduced diffusion coefficient of lithiated graphite (ca. 0.3×10^{-14} m^2 s^{-1} vs. the effective value of 8.0×10^{-14} m^2 s^{-1}) in the very beginning of the short circuit compared to the fitted constant diffusion coefficients used within this work. Based on the altered ratio of diffusion coefficients, the discussed solid phase diffusion limitation within the positive electrode during the transition phase I-II changes toward a solid phase diffusion limitation within the negative electrode at the end of plateau I (compare Figs. 14c to 14f to Figs. 9c to 9f). Associated with the larger solid phase diffusion coefficient of NMC-111 compared to the fitted value, the duration and the C-rate of plateau IIa are over-predicted resulting in an under-prediction of the duration of plateau IIb which, as a consequence, also shows a steeper decrease in predicted C-rate. With the reported high diffusion coefficient of lithiated graphite near complete depletion (ca. 30×10^{-14} m^2 s^{-1}) and the reported low diffusion coefficient of NMC-111 near complete saturation (ca. 0.03×10^{-14} m^2 s^{-1}), a second solid phase diffusion limitation within the negative electrode occurs only at the very end of plateau IIb, indicating the beginning of transition phase II-III. This observation supports the chosen ratio of the fitted constant diffusion coefficients in order to describe the cell's short circuit behavior throughout plateau II and especially IIb. The simulation results suggest that applying diffusion coefficients which vary in the range of up to three orders of magnitude may enhance the prediction accuracy especially at the very beginning of a short circuit, however, the exact behavior must be known for the investigated materials so that the simulation data can also follow the experimentally observed second plateau within which the largest amount of capacity is consumed and which also takes the longest amount of time. Taking into account the experimental data presented by Noh et al.[9] (gray markers in Fig. A1f in the appendix) and Wu et al.[27] (black markers in Fig. A1f in the appendix), a diffusion coefficient ranging between the two might fulfill the requirement of a comparably high diffusion coefficient in the beginning of the short circuit to describe plateau I and the transition phase I-II and a rather low diffusion coefficient at the end to depict the transition from plateau IIa into IIb. The fitted constant diffusion coefficients presented in this work represent effective diffusion coefficients which allow for a surprisingly high prediction accuracy, notwithstanding the simplicity of the approach.

Whilst concentration dependent Li-ion transport parameters within the solid phase are scarcely found in Li-ion battery modeling and simulation,[85] a concentration dependency of parameters describing Li-ion transport within the liquid phase is rather common practice for physical-chemical models describing ion transport throughout the electrodes and separator. To evaluate the relevance of the applied transport properties taken from Valøen and Reimers,[73] the presented data is compared to simulation studies based on liquid phase transport properties taken from Mao et al.,[34] Dees et al.,[74] Nyman et al.,[75] and Lundgren et al.[76] (see Table AIII and Fig. A2 in the appendix) in Fig. 15. As can be seen from from the figure, the liquid phase transport properties mainly affect the magnitude and the duration of the first part of the second plateau (IIa). Mainly following the level of ionic conductivity κ_l and partly also the magnitude of the salt diffusion coefficient D_l, the largest C-rate throughout plateau IIa can be observed for Valøen and Reimers,[73] as well as Mao et al.[34] With an approximately

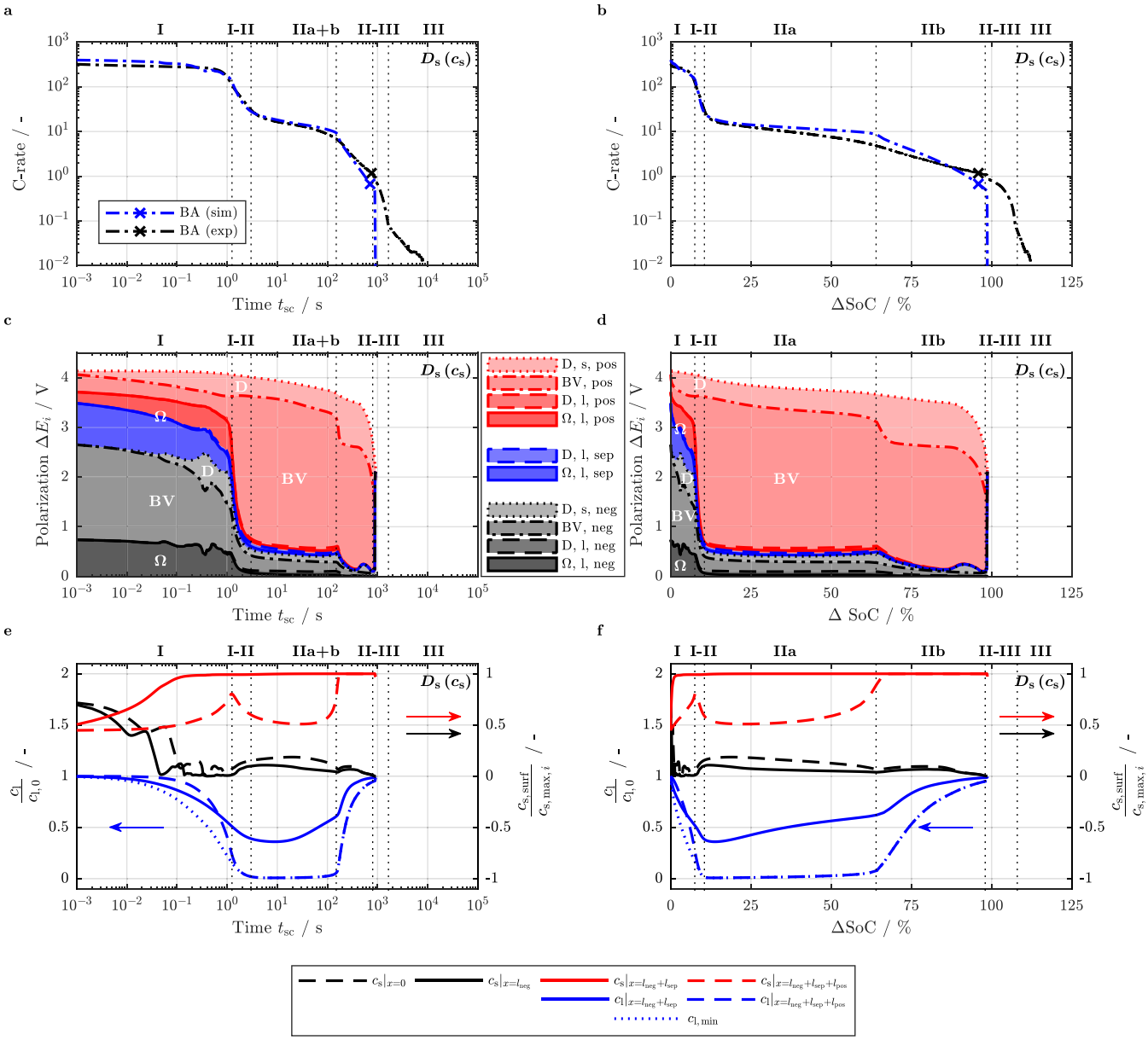

Figure 14. Measured and predicted phases of a short circuit during a 0 V short circuit event for the BA loading at 25°C and an initial cell voltage of 4.15 V observed in C-rate (top: a and b) accounting for concentration dependent solid phase diffusion coefficients D_s (c_s), the corresponding predicted polarization throughout the electrodes and separator (middle: c and d) resulting from the underlying normalized solid (surface) and liquid phase concentration (average) at distinct locations of the cell (bottom: e and f) as a function of short circuit duration (left: a, c, and e) and as a function of normalized discharged capacity (right: b, d, and f).

two times larger ohmic polarization throughout the liquid electrolyte (not explicitly shown here), the simulation data based on Lundgren et al.[76] shows the lowest C-rate throughout plateau IIa. With the ionic conductivity κ_l presented by Dees et al.[74] and Nyman et al.[75] ranging in between, also the C-rate is predicted to lie in this range. With the cation transference number t_+ reported to decrease with increasing salt concentration based on the work of Nyman et al.[75] and Lundgren et al.,[76] the liquid phase diffusion based overpotential in the negative electrode is increasing throughout plateau IIb which, however, seems to have only a minor impact on the transient short circuit behavior despite the predicted maximum salt concentration increasing beyond 4 M (Nyman et al.[75]), even approaching 5 M (Lundgren et al.[76]). Whether such high salt concentrations are even possible without salt precipitation to occur remains unclear. For all other reported data,[34,73,74] the predicted maximum salt concentration ranges below 3 M throughout the short circuit. The simulation data based on the transport properties reported by Mao et al.[34] for an EC:DMC based electrolyte is almost identical to simulation results based on the transport properties taken from Valøen and Reimers,[73] which supports the significance of the applied liquid phase transport properties for the model based short circuit evaluation presented in this work. Interestingly, the choice of the organic solvent used for the $LiPF_6$ based electrolyte seems to have a considerable impact on the dynamics of the short circuit with lower C-rates throughout plateau IIa and, hence, a decelerated energy release below a few hundred seconds or 60% ΔSoC for EC:EMC[74,75] and EC:DEC[76] based electrolytes compared to EC:DMC[34,73] based electrolytes. Whether this is truly the case remains to be evaluated by further experimental work.

Influence of electrode morphology.—As discussed in previous work,[12] a cell that is characterized as high power with thin and/or highly porous electrodes and small active material particles is likely to show an accelerated short circuit behavior compared to a cell that is categorized as high energy with thick and/or dense electrodes and

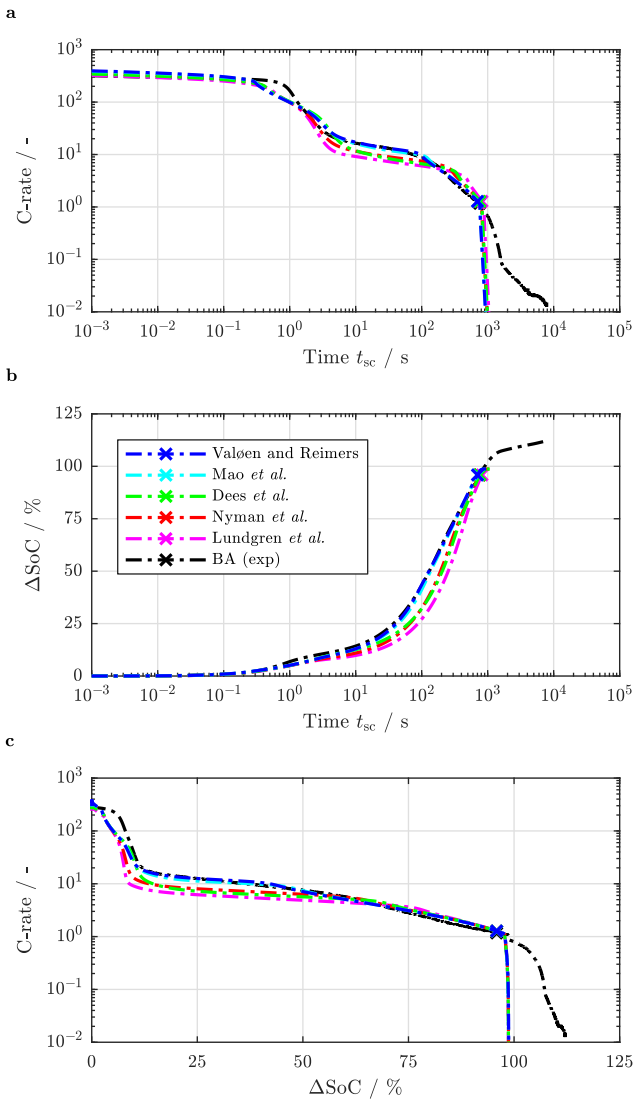

Figure 15. Influence of liquid phase transport properties reported by Valøen and Reimers,[73] Mao et al.,[34] Dees et al.,[74] Nyman et al.,[75] and Lundgren et al.[76] on the electrical cell behavior during a 0 V short circuit event for the BA loading at an initial cell voltage of 4.15 V and 25°C as a function of short circuit duration t_{sc} (a and b) and as a function of normalized discharged capacity ΔSoC (c) for the C-rate (a and c) and ΔSoC (b). Markers indicate 0% SoC.

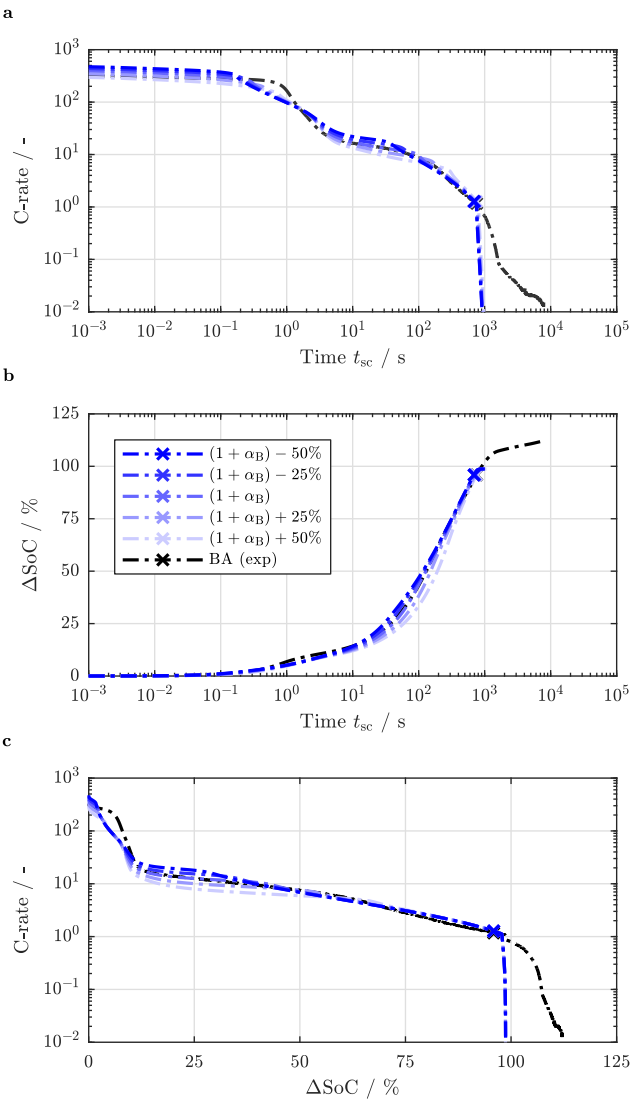

Figure 16. Influence of both positive and negative electrode tortuosity on the electrical cell behavior during a 0 V short circuit event for the BA loading at at an initial cell voltage of 4.15 V and 25°C as a function of short circuit duration t_{sc} (a and b) and as a function of normalized discharged capacity ΔSoC (c) for the C-rate (a and c) and ΔSoC (b). Markers indicate 0% SoC.

large active material particles. In order to evaluate the effect of a cell's energy and power characteristics on its short circuit behavior, the influence of electrode morphology is studied in more detail taking the BA loading as a reference.

Based on the Bruggeman relation, a lower porosity results in a higher tortuosity, thus reducing the effective ionic conductivity $\kappa_{l,\,eff}$ and the effective salt diffusion coefficient $D_{l,\,eff}$ (see Table AI in the appendix). Keeping the active material volume fraction ϵ_s constant in order to not alter the electrode loading, Archie's exponent[90] $(1+\alpha_B)$ within both negative and positive electrode is varied from −50% to +50% as can be seen in Fig. 16. Supporting the observations made from applying different concentration dependent liquid phase transport properties as shown in Fig. 15, primarily the level of plateau IIa is affected by this variation, shifting the beginning of plateau IIb toward earlier or later times for lower or higher tortuosities, respectively. As already observed for varying $LiPF_6$ based electrolytes in Fig. 15, the level of plateau IIb is not influenced by the liquid phase, which implies that cells comprising electrodes with a high tortuosity show a similarly decelerated short circuit behavior as cells which are filled with an electrolyte exhibiting inferior transport properties. Vice versa, cells comprising electrodes with a low tortuosity will show an accelerated short circuit behavior which also becomes apparent throughout plateau I. This observation underlines the importance of effective liquid phase transport properties defining a cell's behavior in the beginning of an external short circuit especially throughout plateau IIa.

With varying the size of both negative and positive active material particles (see Fig. 17), a different behavior can be observed compared to a variation or a scaling of liquid phase transport properties (see Fig. 15 and Fig. 16). Due to the related altered specific surface area within both electrodes, not only the level of plateau I is affected, but also the level of plateau II as a whole is raised or decreased with smaller or larger active material particles, respectively. This becomes especially apparent when looking into the amount of charge withdrawn throughout each plateau IIa and IIb (see Fig. 17c). Plateau IIa varies in a similar fashion as observed for a variation or a scaling of liquid phase transport properties (see Fig. 15c and Fig. 16c). Whilst the predicted level of plateau IIb is unaffected by the liquid phase, it changes with particle size. Reducing the particle size by as much as −50% results in a plateau II which is dominated by phase IIa characterized by a reaction limitation within the positive electrode based on mass transport within both liquid and solid phase. In contrast, increasing the particle size

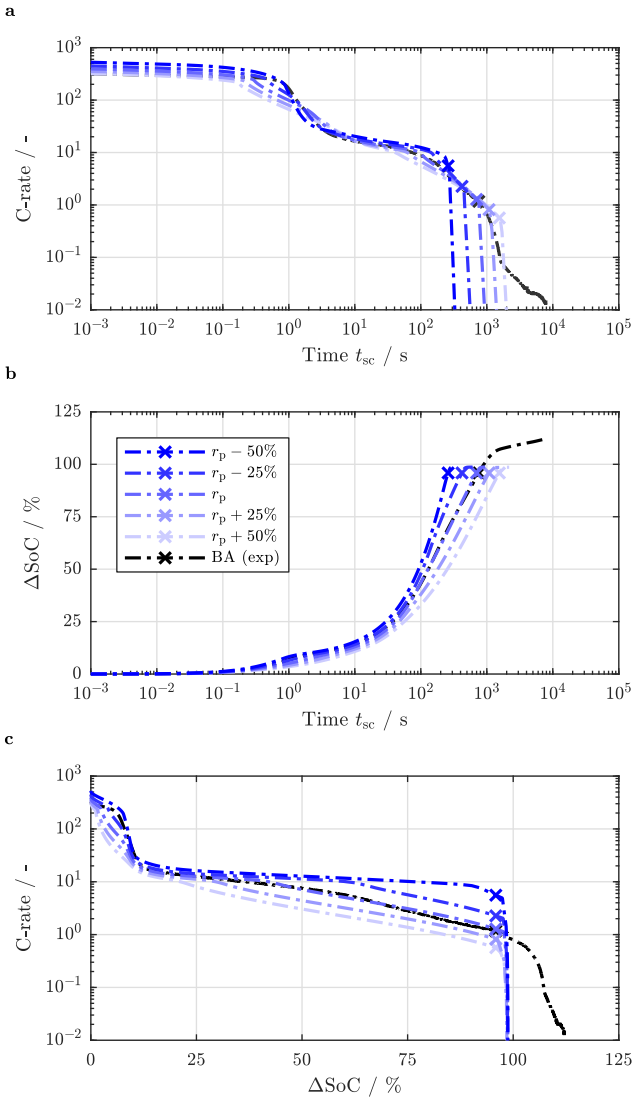

Figure 17. Influence of both positive and negative electrode active material particle size on the electrical cell behavior during a 0 V short circuit event for the BA loading at at an initial cell voltage of 4.15 V and 25°C as a function of short circuit duration t_{sc} (a to d), as a function of normalized discharged capacity ΔSoC (e), and as a function of area specific capacity (f) for the C-rate (a and e), cell current density (b and f), ΔSoC (c), and area specific capacity (d). Markers indicate 0% SoC.

by as much as +50% results in a plateau II which is dominated by phase IIb characterized by a reaction limitation within the positive electrode solely based on mass transport within the solid phase. This variation in dominating mechanisms also affects the amount of time until the cell is completely discharged (see Fig. 17b), which is not the case for a variation or a scaling of liquid phase transport properties (see Fig. 15b and Fig. 16b). This implies that cells comprising large active material particles resulting in a small specific surface area not only increases the share of plateau IIb in plateau II but also reduces the overall level of both plateaus resulting in a slower discharge and, hence, a longer duration until the entire electrical energy is withdrawn from the cell. Analogously, by reducing the particle size, the short circuit is accelerated resulting in a faster discharge and, consequently, faster heat up throughout the entire short circuit.

Lastly, keeping Bruggeman's and, hence, Archie's exponent as well as the active material particle radius constant within both electrodes whilst altering the volume fraction of the solid phase ϵ_s at the expense of porosity ϵ_l, again a slightly different behavior can be observed (see Fig. 18). With the level in C-rate throughout plateau IIb being strongly dependent on the particle radius (see Fig. 17c), it is unaffected by the electrode loading (see Fig. 18e). Reducing the porosity by densifying the electrodes in order to achieve higher electrode loadings at a constant coating thickness, the cell's energy density generally increases. Coming with a reduced porosity, the tortuosity is increased (see Table II) mainly affecting plateau IIa in C-rate. Furthermore, the increased volume fraction of the solid phase also scales the specific surface area available for reaction (see Table AI). Even though the specific surface area is increasing with a reduced porosity which should result in a larger C-rate for higher electrode loadings especially in plateau I (see Fig. 17a), the liquid phase and the associated scaled transport properties are dominating the behavior (see Fig. 18a). Reducing the electrode loading at a constant coating thickness by as much as −50% results in a dominating plateau IIb throughout almost the entire short circuit duration skipping plateau IIa which sets kind of a limit to the dynamics of the short circuit based on the employed active materials (see Fig. 18e). By increasing the electrode loading by as much as +50%, plateau IIa is dominating instead resulting in a suppression of plateau IIb. The lack of plateau IIb results in a strongly decelerated short circuit behavior throughout the entire duration of the short circuit implying a slower release of the stored specific electrical and, hence, thermal energy (see Fig. 18c). This does not only account for the C-rate and ΔSoC but also for the cell current density i_{sc} (mA cm^{-2}) and area specific discharged capacity C_{sc}/A (mA cm^{-2}) as shown on the right of Figs. 18b,18d, and 18f. This behavior is differing from the observed characteristics of the HP, BA, and HE loading which show the same sequence of plateaus unaffected by the area specific capacity (compare Fig. 18c to Fig. 3c). This effect can be explained by the applied strongly varying porosities (ca. 75% to 25% for −50% to +50% in capacity) based on the altered volume fractions of the active materials affecting electrode tortuosity, whilst fairly constant porosities and solid phase volume fractions were observed for the HP, BA, and, HE loading mainly varying in coating thickness (see Table II).

This sensitivity analysis underlines the importance of electrochemically engineered electrodes and cells that may allow for designing Li-ion cells which, on the one hand, comply with the energy and power characteristics required by a given application and, on the other hand, show a maximized level of safety during short circuit events. The complex interplay between transport properties within the cell's solid an liquid components and the morphology of the electrodes and separator, however, needs to be thoroughly evaluated to achieve this task.

By adapting the model parameters, not only the impact of different electrode morphologies and electrolytes can be described, but also different active materials such as the increasingly prominent combination of silicon-graphite compounds and nickel-rich layered oxides can be investigated in terms of the short circuit characteristics.[91] By further combining the presented p2D physical-chemical model with an electrical model describing the potential and current density distribution within the current collectors[72,92] as well a thermal model accounting for a temperature distribution within the cell's jelly roll or electrode stack,[91,92] also large-format Li-ion cells can be described during short circuit events. Such a combined modeling approach might help to identify critical short circuit conditions, which could result in the occurrence of thermal decomposition reactions and ultimately thermal runaway at a certain combination of temperature and SoC reached throughout the short circuit.[64] This information could be further used to design cells and electrodes depending on the topology of the battery pack with its inherent thermal management system in order to maximize the short circuit tolerance of the entire battery system.

Conclusions

Within this work, experimental data from quasi-isothermal external short circuit tests applied to single-layered pouch-type Li-ion cells with graphite anodes and NMC-111 cathodes published in the first part of this combined work was used to validate a well-known physical-chemical model at very high currents. Based on this validated model, the underlying mechanisms occurring within the electrodes and separator during external short circuit tests were evaluated. The impact of

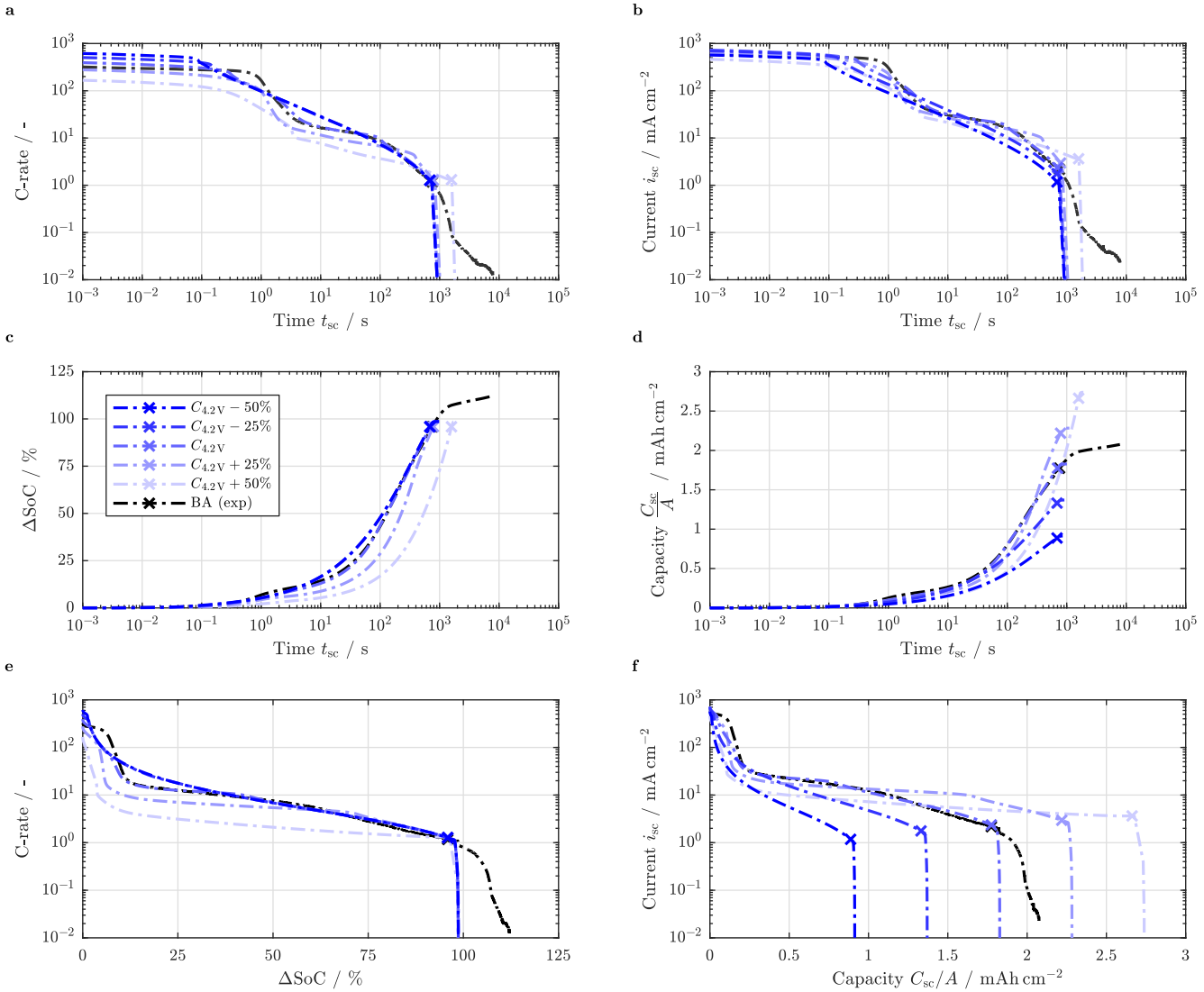

Figure 18. Influence of both positive and negative electrode loading at a constant coating thickness on the electrical cell behavior during a 0 V short circuit event for the BA loading at an initial cell voltage of 4.15 V and 25°C as a function of short circuit duration t_{sc} (a and b) and as a function of normalized discharged capacity ΔSoC (c) for the C-rate (a and c) and ΔSoC (b). Markers indicate 0% SoC.

transport properties reported in literature for both the liquid electrolyte and the solid active material particles was studied by means of a sensitivity analysis which was concluded by considerations on the effect of a cell's energy and power characteristics on its short circuit dynamics.

In order to guarantee a smooth calculation of the cell's short circuit behavior when using a commercial solver, a previously suggested modification of the Butler-Volmer equation based on a diffusion limitation within the liquid electrolyte was evaluated and extended by accounting for an additional solid phase diffusion limitation within both the negative and positive electrode. By means of this slight modification, applying liquid phase transport properties which depend on the local salt concentration and temperature, combined with effective solid phase diffusion coefficients depending solely on stoichiometry or electrode balancing as well as temperature, can reproduce the electrical and thermal short circuit behavior of a cell very well, with only minor discrepancies at the very beginning of a short circuit.

The three distinct plateaus which can be observed in a double-logarithmic representation of the short circuit current and heat generation rate as a function of time were correlated to the model-predicted underlying Li-ion concentration distribution throughout the electrodes as well as electrolyte and separator. Each of the three plateaus is characterized by distinct transport limitations within the solid and/or liquid phase within both electrodes which affect reaction kinetics and define the level in current and heat generation rate of each plateau. Accompanied with the analysis of the concentration distribution at distinct positions along the electrodes and separator, the cell polarization based on ohmic and diffusion related effects as well as reaction kinetics was calculated and shown to agree with previously published findings. Whilst the first plateau is characterized by comparably large ohmic losses within the liquid electrolyte accompanied with very large currents as well as a reaction limitation within the negative electrode, the second plateau is based on a distinct limitation in mass transport within the liquid and/or solid phase increasing the reaction overpotential in the positive electrode. In an SoC based representation of the short circuit behavior, the second plateau can be further divided into two parts, with the second part shown to be dominated by solid phase diffusion within the positive electrode allowing to determine effective solid phase diffusion coefficients. The previously stated theory[12] that the experimentally observed third and last plateau can be partially attributed to an anodic dissolution reaction of the copper current collector within the negative electrode, was supported by simulated anode potentials exceeding 3.1 V vs. Li/Li$^+$ at the end of the discharge.

The observed minor discrepancies between predicted and measured cell behavior at the very beginning of the short circuit could be ruled out by applying solid phase diffusion coefficients within both the negative and positive electrode depending on the local

Li-ion concentration within the active material particles. However, the exact dependency of the solid phase diffusion coefficients on Li-ion concentration needs to be known to also be able to properly describe the cell's behavior during the second plateau which is dominating the electrical and thermal short circuit behavior of the investigated cells.

Similar to varying liquid phase transport properties reported in literature for electrolytes based on $LiPF_6$ and organic solvents, the tortuosity scaling the ionic conductivity and salt diffusion coefficient mainly affects the first part of the second plateau with lower currents and heat generation rates for electrolytes showing inferior transport properties or electrodes with a high tortuosity. Increasing the size of the active material particles, the current and heat generation rate throughout the second part of the second plateau is reduced. By further increasing the electrode loading whilst keeping the coating thickness constant at the expense of porosity, resulting in a higher energy density of the cell, the level of the first part of the second plateau is reduced whilst its share throughout the second plateau is increased. Varying the electrode loading by increasing the coating thickness whilst keeping the electrode morphology constant affects the level of the first and second plateau as a whole whilst the ratio between the first part and the second part of the second plateau is unchanged.

These observations support the assumption that cells which can be characterized as high energy with thick and/or dense electrodes as well as large active material particles will result in a decelerated short circuit behavior compared to cells which can be described high power with thin and/or highly porous electrodes as well as small active material particles. Combining simulation studies with experiments ranging from normal operation to high performance and abusive scenarios may allow for designing electrodes and cells with a high energy density which can deliver the required rate capability at a maximum level of safety. This combined approach should be further investigated by experimentally validated modeling and simulation investigating not only the rate capability of materials, electrodes, and cells from normal to abusive conditions but also studying the thermal stability of the used components as well as the heat generated during operation. With such a validated model describing both the electrical and thermal safety characteristics for a combination of materials and electrodes, a truly conclusive electrode and cell design study can be carried out. Furthermore, the methodology presented within this combined work should be extended toward quasi-isothermal internal short circuit tests which will be the subject of future work.

Appendix

In order to be able to reproduce the simulation results presented in this work, the underlying model equations of the applied p2D model as well as parameters describing both liquid and solid phase are summarized.

Model equations.—In Table AI, an overview of main variables describing the Li-ion concentration c (mol m^{-3}) and the potential Φ vs. Li/Li$^+$ (V) of both liquid (l) and solid phase (s) associated with each computational domain is given. Furthermore, governing

Table AI. Main variables, governing partial differential equations, and additional analytic expressions solved within each domain of the p2D physical-chemical model as well as prevailing boundary and initial conditions.

Description	Negative electrode (neg) Graphite	Separator (sep) Polyolefin	Positive electrode (pos) NMC-111
Variables	$c_\mathrm{l}(x,t)$, $c_\mathrm{s}(x,r,t)$, $\Phi_\mathrm{l}(x,t)$, $\Phi_\mathrm{s}(x,t)$ $x \in [0; l_\mathrm{neg}]$ $r \in [0; r_\mathrm{p,\,neg}]$	$c_\mathrm{l}(x,t)$, $\Phi_\mathrm{l}(x,t)$ $x \in [l_\mathrm{neg}; l_\mathrm{neg}+l_\mathrm{sep}]$	$c_\mathrm{l}(x,t)$, $c_\mathrm{s}(x,r,t)$, $\Phi_\mathrm{l}(x,t)$, $\Phi_\mathrm{s}(x,t)$ $x \in [l_\mathrm{neg}+l_\mathrm{sep}; l_\mathrm{neg}+l_\mathrm{sep}+l_\mathrm{pos}]$ $r \in [0; r_\mathrm{p,\,pos}]$
Governing partial differential equations			
Mass balance (liquid)	$\epsilon_\mathrm{l,neg}\frac{\partial c_\mathrm{l}}{\partial t} = \nabla(D_\mathrm{l,eff}\nabla c_\mathrm{l}) - \nabla\left(\frac{\mathbf{i}_\mathrm{l}(1-t_+)}{F}\right)$	$\epsilon_\mathrm{l,sep}\frac{\partial c_\mathrm{l}}{\partial t} = \nabla(D_\mathrm{l,eff}\nabla c_\mathrm{l})$	$\epsilon_\mathrm{l,pos}\frac{\partial c_\mathrm{l}}{\partial t} = \nabla(D_\mathrm{l,eff}\nabla c_\mathrm{l}) - \nabla\left(\frac{\mathbf{i}_\mathrm{l}(1-t_+)}{F}\right)$
Mass balance (solid)	$\frac{\partial c_\mathrm{s}}{\partial t} = \frac{1}{r^2}\frac{\partial}{\partial r}\left(D_\mathrm{s,\,neg} r^2 \frac{\partial c_\mathrm{s}}{\partial r}\right)$	n/a	$\frac{\partial c_\mathrm{s}}{\partial t} = \frac{1}{r^2}\frac{\partial}{\partial r}\left(D_\mathrm{s,\,pos} r^2 \frac{\partial c_\mathrm{s}}{\partial r}\right)$
Ohm's law (liquid)	$\mathbf{i}_\mathrm{l} = -\kappa_\mathrm{l,\,eff}\nabla\Phi_\mathrm{l} + \frac{2\kappa_\mathrm{l,\,eff}RT}{F}(1-t_+)\left(1+\frac{\partial \ln f_\pm}{\partial \ln c_\mathrm{l}}\right)\nabla \ln c_\mathrm{l}$		
Ohm's law (solid)	$\mathbf{i}_\mathrm{s} = -\sigma_\mathrm{s,\,eff}\nabla\Phi_\mathrm{s}$	n/a	$\mathbf{i}_\mathrm{s} = -\sigma_\mathrm{s,\,eff}\nabla\Phi_\mathrm{s}$
Charge balance	$\nabla\mathbf{i}_\mathrm{l} = -\nabla\mathbf{i}_\mathrm{s} = \frac{3\epsilon_\mathrm{s,\,neg}}{r_\mathrm{p,\,neg}} i_\mathrm{n}$	$\nabla\mathbf{i}_\mathrm{l} = 0$	$\nabla\mathbf{i}_\mathrm{l} = -\nabla\mathbf{i}_\mathrm{s} = \frac{3\epsilon_\mathrm{s,\,pos}}{r_\mathrm{p,\,pos}} i_\mathrm{n}$
Additional analytic expressions			
Ionic diffusivity	$D_\mathrm{l,\,eff} = \frac{\epsilon_\mathrm{l,\,neg}}{\tau_\mathrm{neg}} D_\mathrm{l}$	$D_\mathrm{l,\,eff} = \frac{\epsilon_\mathrm{l,\,sep}}{\tau_\mathrm{sep}} D_\mathrm{l}$	$D_\mathrm{l,\,eff} = \frac{\epsilon_\mathrm{l,\,pos}}{\tau_\mathrm{pos}} D_\mathrm{l}$
Ionic conductivity	$\kappa_\mathrm{l,\,eff} = \frac{\epsilon_\mathrm{l,\,neg}}{\tau_\mathrm{neg}} \kappa_\mathrm{l}$	$\kappa_\mathrm{l,\,eff} = \frac{\epsilon_\mathrm{l,\,sep}}{\tau_\mathrm{sep}} \kappa_\mathrm{l}$	$\kappa_\mathrm{l,\,eff} = \frac{\epsilon_\mathrm{l,\,pos}}{\tau_\mathrm{pos}} \kappa_\mathrm{l}$
Electronic conductivity	$\sigma_\mathrm{s,\,eff} = \epsilon_\mathrm{s,\,neg}\sigma_\mathrm{s,\,neg}$	n/a	$\sigma_\mathrm{s,\,eff} = \epsilon_\mathrm{s,\,pos}\sigma_\mathrm{s,\,pos}$
Reaction kinetics	$i_\mathrm{n} = \frac{i_0\left[\exp\left(\frac{\alpha_\mathrm{a}F}{RT}\eta\right) - \exp\left(\frac{\alpha_\mathrm{c}F}{RT}\eta\right)\right]}{1+\frac{c_\mathrm{s,\,lim}}{\Delta c_\mathrm{s}}\exp\left(\frac{\alpha_\mathrm{a}F}{RT}\eta\right)}$	n/a	$i_\mathrm{n} = \frac{i_0\left[\exp\left(\frac{\alpha_\mathrm{a}F}{RT}\eta\right) - \exp\left(\frac{\alpha_\mathrm{c}F}{RT}\eta\right)\right]}{1+\left(\frac{c_\mathrm{l,\,lim}}{\Delta c_\mathrm{l}} + \frac{c_\mathrm{s,\,lim}}{\Delta c_\mathrm{s}}\right)\exp\left(\frac{\alpha_\mathrm{c}F}{RT}\eta\right)}$
Exchange current density	$i_0 = Fk_\mathrm{neg}\left(\frac{c_\mathrm{l}}{c_\mathrm{l,\,ref}}\right)^{\alpha_\mathrm{a}}\left(c_\mathrm{s,\,max,\,neg} - c_\mathrm{s,\,surf}\right)^{\alpha_\mathrm{a}}\left(c_\mathrm{s,\,surf}\right)^{\alpha_\mathrm{c}}$	n/a	$i_0 = Fk_\mathrm{pos}\left(\frac{c_\mathrm{l}}{c_\mathrm{l,\,ref}}\right)^{\alpha_\mathrm{a}}\left(c_\mathrm{s,\,max,\,pos} - c_\mathrm{s,\,surf}\right)^{\alpha_\mathrm{a}}\left(c_\mathrm{s,\,surf}\right)^{\alpha_\mathrm{c}}$
Reaction overpotential	$\eta = \Phi_\mathrm{s} - \Phi_\mathrm{l} - \Delta\Phi_\mathrm{s,\,film} - E_\mathrm{eq,\,neg}$	n/a	$\eta = \Phi_\mathrm{s} - \Phi_\mathrm{l} - E_\mathrm{eq,\,pos}$
Boundary conditions[*]			
Species 2nd (liquid)	$\nabla c_\mathrm{l}\vert_{x=0} = 0$	n/a	$\nabla c_\mathrm{l}\vert_{x=l_\mathrm{neg}+l_\mathrm{sep}+l_\mathrm{pos}} = 0$
Species 2nd (solid)	$\frac{\partial c_\mathrm{s}}{\partial r}\Big\vert_{r=0} = 0 \quad \frac{\partial c_\mathrm{s}}{\partial r}\Big\vert_{r=r_\mathrm{p,\,neg}} = -\frac{i_\mathrm{n}}{FD_\mathrm{s,\,neg}}$	n/a	$\frac{\partial c_\mathrm{s}}{\partial r}\Big\vert_{r=0} = 0 \quad \frac{\partial c_\mathrm{s}}{\partial r}\Big\vert_{r=r_\mathrm{p,\,pos}} = -\frac{i_\mathrm{n}}{FD_\mathrm{s,\,pos}}$
Potential 2nd (liquid)	$\nabla\Phi_\mathrm{l}\vert_{x=0} = 0$	n/a	$\nabla\Phi_\mathrm{l}\vert_{x=l_\mathrm{neg}+l_\mathrm{sep}+l_\mathrm{pos}} = 0$
Potential 1st (solid)	$\Phi_\mathrm{s}\vert_{x=0} = 0$	n/a	[**] $\Phi_\mathrm{s}\vert_{x=l_\mathrm{neg}+l_\mathrm{sep}+l_\mathrm{pos}} = 10^{-6}$ V
Potential 2nd (solid)	$\nabla\Phi_\mathrm{s}\vert_{x=l_\mathrm{neg}} = 0$	n/a	$\nabla\Phi_\mathrm{s}\vert_{x=l_\mathrm{neg}+l_\mathrm{sep}} = 0$ [**] $\nabla\Phi_\mathrm{s}\vert_{x=l_\mathrm{neg}+l_\mathrm{sep}+l_\mathrm{pos}} = -\frac{E_\mathrm{cell}}{R_\mathrm{ext}\sigma_\mathrm{s,\,eff}}$
Initial conditions			
Species (liquid)		$c_\mathrm{l}(x, t=0) = c_\mathrm{l,\,0}$	
Species (solid)	$c_\mathrm{s}(x,r,t=0) = c_\mathrm{s,\,0,\,neg}$	n/a	$c_\mathrm{s}(x,r,t=0) = c_\mathrm{s,\,0,\,pos}$
Potential (liquid)		$\Phi_\mathrm{l}(x, t=0) = -E_\mathrm{eq,\,neg}$	
Potential (solid)	$\Phi_\mathrm{s}(x, t=0) = 0$		$\Phi_\mathrm{s}(x, t=0) = E_\mathrm{eq,\,pos} - E_\mathrm{eq,\,neg}$

[*] indicated as first (Dirichlet) and second order (Neumann) boundary conditions.
[**] alternatively used for constant voltage (Dirichlet) and constant resistance (Neumann) short circuit conditions.

Table AII. Equation overview for calculating the overall polarization within each domain of the p2D physical-chemical model based on mass and charge transport as well as reaction kinetics.

Description	Symbol	Negative electrode (neg) Graphite	Separator (sep) Polyolefin	Positive electrode (pos) NMC-111
Definitions				
Bounds of integration	l_1	l_{neg}	$l_{neg}+l_{sep}$	$l_{neg}+l_{sep}+l_{pos}$
	l_0	0	l_{neg}	$l_{neg}+l_{sep}$
Specific surface	a	$\frac{3\epsilon_{s,\,neg}}{r_{p,\,neg}}$	n/a	$\frac{3\epsilon_{s,\,pos}}{r_{p,\,pos}}$
Total current	i_{tot}	$\int_{l_0}^{l_1}(a i_n)\,dx$	n/a*	$\int_{l_0}^{l_1}(a i_n)\,dx$
Polarization expressions				
Diffusion polarization (liquid)	$\Delta E_{D,\,l}$	$-\frac{1}{i_{tot}}\int_{l_0}^{l_1}\left(\mathbf{i}_l\frac{2RT}{F}(1-t_+)\left(1+\frac{\partial \ln f_\pm}{\partial \ln c_l}\right)\nabla \ln c_l\right)dx$		
Diffusion polarization (solid)	$\Delta E_{D,\,s}$	$\frac{1}{i_{tot}}\int_{l_0}^{l_1}\left(a i_n\left(E_{eq,\,neg}-E_{eq,\,neg,\,ave}\right)\right)dx$	n/a	$\frac{1}{i_{tot}}\int_{l_0}^{l_1}\left(a i_n\left(E_{eq,\,pos}-E_{eq,\,pos,\,ave}\right)\right)dx$
Ohmic losses (liquid)	$\Delta E_{\Omega,\,l}$	$\frac{1}{i_{tot}}\int_{l_0}^{l_1}\left(\frac{\mathbf{i}_l^2}{\kappa_{l,\,eff}}\right)dx$		
Ohmic losses (solid)	$\Delta E_{\Omega,\,s}$	$\frac{1}{i_{tot}}\int_{l_0}^{l_1}\left(\frac{\mathbf{i}_s^2}{\sigma_{s,\,eff}}\right)dx$	n/a	$\frac{1}{i_{tot}}\int_{l_0}^{l_1}\left(\frac{\mathbf{i}_s^2}{\sigma_{s,\,eff}}\right)dx$
Reaction overpotential	ΔE_{BV}	$\frac{1}{i_{tot}}\int_{l_0}^{l_1}\left(a i_n\left(\Phi_s-\Phi_l-E_{eq,\,neg}\right)\right)dx$	n/a	$\frac{1}{i_{tot}}\int_{l_0}^{l_1}\left(a i_n\left(\Phi_s-\Phi_l-E_{eq,\,pos}\right)\right)dx$
Overall polarization	$\sum\Delta E$	$\Delta E_{D,\,l}+\Delta E_{D,\,s}+\Delta E_{\Omega,\,l}+\Delta E_{\Omega,\,s}+\Delta E_{BV}$	$\Delta E_{D,\,l}+\Delta E_{\Omega,\,l}$	$\Delta E_{D,\,l}+\Delta E_{D,\,s}+\Delta E_{\Omega,\,l}+\Delta E_{\Omega,\,s}+\Delta E_{BV}$

*calculated total current within the positive electrode is used.

partial differential equations describing both mass and charge transport throughout the negative (neg) and positive electrode (pos) as well as the separator (sep) whilst accounting for a charge balance between both solid and liquid components are summarized. Together with additional analytical expressions describing effective transport parameters and reaction kinetics as well as the presented boundary and initial conditions, the model is fully described.

In order to evaluate the contribution of each underlying mechanism to the total polarization of the cell ΔE_{cell} (V), each individual voltage loss is calculated according to Nyman et al.[26] following the work of Rao and Newman[69] within all three domains as shown in Table AII. Based on the contribution of diffusion related losses (D) and ohmic losses (Ω) within the solid and liquid components of the cell as well as overpotentials associated with Butler-Volmer reaction kinetics (BV), the overall polarization $\sum\Delta E$ (V) within each electrode as well as the voltage drop across the separator can be calculated. Hence, the total polarization ΔE_{cell} occurring within the cell can be determined via[75]

$$\Delta E_{cell} = -\sum\Delta E_{neg}+\sum\Delta E_{sep}+\sum\Delta E_{pos} \quad [A1]$$

Essentially, ΔE_{cell} can be further calculated as[75]

$$\Delta E_{cell} = E_{cell}-E_{eq,\,cell,\,ave} = \Phi_s|_{l_{1,\,pos}}-\Phi_s|_{l_{0,\,neg}}+ -\frac{1}{i_{tot,\,pos}}\int_{l_{0,\,pos}}^{l_{1,\,pos}}\left(a_{pos}\,i_n\,E_{eq,\,pos,\,ave}\right)dx+ +\frac{1}{i_{tot,\,neg}}\int_{l_{0,\,neg}}^{l_{1,\,neg}}\left(a_{neg}\,i_n\,E_{eq,\,neg,\,ave}\right)dx \quad [A2]$$

with the average equilibrium potentials $E_{eq,\,neg,\,ave}$ and $E_{eq,\,pos,\,ave}$ vs. Li/Li^+ (V) occurring after an infinitely long relaxation period being a function of the average concentration within the active material particles $c_{s,\,ave}$. In contrast, the equilibrium potentials characterizing the reaction site $E_{eq,\,neg}$ and $E_{eq,\,pos}$ vs. Li/Li^+ are defined by the surface concentration of the active material particles $c_{s,\,surf}$. Both equations shown in Eq. A1 and Eq. A2 come to the same result which underlines the plausibility of the polarization expressions stated by Nyman et al.[75] even at very high currents.

Based on irreversible and reversible contributions neglecting heat of mixing effects,[34,68,69,93] the overall heat generation rate $\dot{q}_{cell}$ ($W\,m^{-2}$) can be approximated via

$$\dot{q}_{cell} = \dot{q}_{irrev,\,cell}+\dot{q}_{rev,\,cell} = \left(\dot{q}_{irrev,\,neg}+\dot{q}_{irrev,\,sep}+\dot{q}_{irrev,\,pos}\right)+\left(\dot{q}_{rev,\,neg}+\dot{q}_{rev,\,pos}\right) \quad [A3]$$

Together with the cell current density i_{cell} ($A\,m^{-2}$) as shown in Table AII

$$i_{cell} = i_{tot,\,pos} = -i_{tot,\,neg} \quad [A4]$$

the irreversible heat generation rate within the cell $\dot{q}_{irrev,\,cell}$ calculates as

$$\dot{q}_{irrev,\,cell} = i_{cell}\,\Delta E_{cell} = i_{cell}\,E_{cell}-\int_{l_{0,\,neg}}^{l_{1,\,neg}}\left(a_{neg}\,i_n\,E_{eq,\,neg,\,ave}\right)dx+ -\int_{l_{0,\,pos}}^{l_{1,\,pos}}\left(a_{pos}\,i_n\,E_{eq,\,pos,\,ave}\right)dx \quad [A5]$$

whereas the overall reversible heat generation rate $\dot{q}_{rev,\,cell}$ is estimated via

$$\dot{q}_{rev,\,cell} = \int_{l_{0,\,neg}}^{l_{1,\,neg}}\left(a_{neg}\,i_n\,T\,\frac{dE_{eq,\,neg,\,ave}}{dT}\right)dx+\int_{l_{0,\,pos}}^{l_{1,\,pos}}\left(a_{pos}\,i_n\,T\,\frac{dE_{eq,\,pos,\,ave}}{dT}\right)dx \quad [A6]$$

with the entropic coefficients $\frac{dE_{eq,\,neg,\,ave}}{dT}$ and $\frac{dE_{eq,\,pos,\,ave}}{dT}$ ($V\,K^{-1}$) of the negative and positive active materials which results in the often cited form[68]

$$\dot{q}_{cell} = \left[i_{cell}\,E_{cell}-\left(\int_{l_{0,\,neg}}^{l_{1,\,neg}}\left(a_{neg}\,i_n\,E_{eq,\,neg,\,ave}\right)dx+\int_{l_{0,\,pos}}^{l_{1,\,pos}}\left(a_{pos}\,i_n\,E_{eq,\,pos,\,ave}\right)dx\right)\right]+ +\left(\int_{l_{0,\,neg}}^{l_{1,\,neg}}\left(a_{neg}\,i_n\,T\,\frac{dE_{eq,\,neg,\,ave}}{dT}\right)dx+\int_{l_{0,\,pos}}^{l_{1,\,pos}}\left(a_{pos}\,i_n\,T\,\frac{dE_{eq,\,pos,\,ave}}{dT}\right)dx\right) \quad [A7]$$

Pre-studies have shown that despite the large currents, the contribution of heat of mixing effects within the active material particles approximated in accordance with Thomas and Newman[93] is ranging below the contribution of entropy related effects throughout the short circuit which is why it is not considered here.

Within this work, $\dot{q}_{sc} = \dot{q}_{tot}$ and $i_{sc} = -i_{cell}$. Together with the electrode area A of the experimentally investigated pouch-type cells (ca. 31 mm × 56 mm), the overall heat generation rate $\dot{Q}_{sc}$ (W) and short circuit current I_{sc} (A) can be calculated.

Solid phase parameters.—Applied half-cell potentials derived from averaging between lithiation and delithiation during a C/50 constant current operation are shown in Fig. A1a and A1b for the negative and positive electrode. The entropic coefficient of Li_xC was taken from experimental data reported by Reynier et al.[70] directly measuring the variation of the half-cell potential vs. Li/Li^+ with temperature. The entropic coefficient $\frac{dE_{eq,\,neg}}{dT}$ ($V\,K^{-1}$) was fitted according to Eq. A8 as a function of degree of lithiation x which is shown in Fig. A1c (solid line) together with the underlying experimental data (markers).

$$\frac{dE_{eq,\,neg}}{dT} = \frac{-3.8149\times10^{-4}x^5+1.058\times10^{-3}x^4-1.1235\times10^{-3}x^3+5.5727\times10^{-4}x^2-1.242\times10^{-4}x+9.0095\times10^{-6}}{x^5-2.9967x^4+3.2192x^3-1.4066x^2+1.8475\times10^{-1}x+1.3198\times10^{-2}} \quad [A8]$$

Similarly, experimental data gained from isothermal microcalorimetry reported by Lu et al.[71] was used for describing the entropic coefficient of $Li_yNi_{1/3}Co_{1/3}Mn_{1/3}O_2$. The entropic coefficient $\frac{dE_{eq,\,pos}}{dT}$ ($V\,K^{-1}$) was fitted according to Eq. A9 as a function of degree of lithiation y which is shown in Fig. A1d (solid line) together with the underlying experimental data (markers).

$$\frac{dE_{eq,\,pos}}{dT} = \frac{-2.445\times10^{-3}y^2+3.4961\times10^{-3}y-1.4125\times10^{-3}}{y^2-2.7564y+3.9766} \quad [A9]$$

To describe a solid phase diffusion within the active material particles depending on a diffusion coefficient varying with Li-ion concentration along the pseudo-dimension r, experimental work of Levi and Aurbach[77] as well as Wu et al.[27] were used for Li_xC

Table AIII. Fitting functions for liquid phase transport properties based on electrolyte salt concentration c_l (mol m^{-3}) and temperature T (K).

Equation / Parameter	Valøen and Reimers[73] PC:EC:DMC 10:27:63 (vol:vol:vol)	Mao et al.[34] EC:DMC 1:1 (n/a:n/a)	Dees et al.[74] EC:EMC 3:7 (wt:wt)	Nyman et al.[75] EC:EMC 3:7 (wt:wt)	Lundgren et al.[76] EC:DEC 1:1 (wt:wt)
Ionic conductivity κ_l (S m^{-1})					
$\kappa_l = k_1 \cdot \left(\frac{c_l}{k_2}\right)^{(k_3-1)} \cdot \exp\left(-\left(\frac{c_l}{k_2}\right)^{k_3}\right)$ with $k_i = k_{i1}\exp\left(-\frac{k_{i2}}{T}\right)$					
k_{11}	4.7557×10^2	7.2999×10^2	9.0924×10^2	2.0743×10^0	8.9364×10^2
k_{12}	1.5570×10^3	1.6900×10^3	1.8246×10^3	0	1.8601×10^3
k_{21}	1.1730×10^4	2.0500×10^3	6.3255×10^3	1.6437×10^3	1.1258×10^4
k_{22}	5.7251×10^2	0	3.9753×10^2	0	5.9703×10^2
k_{31}	1.73	1.73	1.8	1.71	1.71
k_{32}	0	0	0	0	0
Salt diffusion coefficient D_l (m^2 s^{-1}):					
$D_l = d_1 \cdot \exp\left(-d_2 \cdot c_l + \frac{d_3}{d_4 + d_5 \cdot c_l - T}\right)$					
d_1	3.7290×10^{-9}	4.3880×10^{-7}	1.7041×10^{-5}	5.8289×10^{-10}	8.5689×10^{-9}
d_2	5.0646×10^{-4}	6.5000×10^{-4}	1.9023×10^{-4}	1.2626×10^{-3}	1.1645×10^{-3}
d_3	1.2500×10^2	2.0000×10^3	3.4528×10^3	0	8.9000×10^2
d_4	2.2879×10^2	0	-1.6595×10^1	0	0
d_5	5.0051×10^{-3}	0	1.6520×10^{-2}	0	0
Cation transference number t_+:					
$t_+ = t_1 + t_2 \cdot \tanh\left(\frac{c_l - t_3}{t_4}\right) + t_5 \cdot \tanh\left(\frac{c_l - t_6}{t_7}\right)$ with $t_i = t_{i1} \cdot \exp\left(\frac{t_{i2}}{t_{i3} - T}\right)$					
t_{11}	0.38	0.4	1.3742×10^0	2.7466×10^{-1}	5.2307×10^{-1}
t_{12}	0	0	3.8936×10^3	0	4.7331×10^{-2}
t_{13}	0	0	-3.0559×10^3	0	1.0137×10^0
t_{21}	0	0	4.9427×10^{-3}	-1.2798×10^{-1}	8.6228×10^0
t_{22}	0	0	-3.0545×10^3	0	0
t_{23}	0	0	-1.0117×10^3	0	0
t_{31}	0	0	-1.7559×10^3	1.9687×10^3	1.9319×10^3
t_{32}	0	0	1.7984×10^2	0	3.7635×10^2
t_{33}	0	0	1.9686×10^2	0	1.0734×10^2
t_{41}	0	0	5.3158×10^3	4.2195×10^2	9.3645×10^2
t_{42}	0	0	2.4728×10^2	0	1.4192×101
t_{43}	0	0	5.3978×10^1	0	2.3004×10^2
t_{51}	0	0	0	-1.4669×10^{-1}	-9.1458×10^0
t_{52}	0	0	0	0	0
t_{53}	0	0	0	0	0
t_{61}	0	0	0	9.5080×10^1	1.9067×10^3
t_{62}	0	0	0	0	3.7232×10^2
t_{63}	0	0	0	0	1.1446×10^2
t_{71}	0	0	0	4.6829×10^2	9.7011×10^2
t_{72}	0	0	0	0	1.5087×10^1
t_{73}	0	0	0	0	2.2748×10^2
Thermodynamic factor TDF:					
$(1-t_+) \cdot \mathrm{TDF} = (1-t_+) \cdot \left(1 + \frac{\partial \ln f_\pm}{\partial \ln c_l}\right) = f_1 \cdot c_l{}^{p_1} + f_2 \cdot c_l{}^{p_2} + f_3$ with $f_i = f_{i1} \cdot \exp\left(\frac{f_{i2}}{f_{i3} - T}\right)$					
p_1	1.5	0	2	2	2
p_2	0.5	0	1	1	1
f_{11}	2.4174×10^{-3}	0.6	2.7539×10^{-7}	2.8687×10^{-7}	7.8994×10^{-6}
f_{12}	-3.3972×10^3	0	-3.3210×10^2	0	1.0027×10^3
f_{13}	1.0732×10^3	0	0	0	0
f_{21}	-7.5895×10^{-3}	0	-1.5756×10^{-7}	7.4678×10^{-4}	2.8106×10^{-2}
f_{22}	0	0	-1.8453×10^3	0	1.1294×10^3
f_{23}	0	0	0	0	0
f_{31}	6.0100×10^{-1}	0	1.7116×10^{-1}	4.4103×10^{-1}	9.2607×10^{-1}
f_{32}	0	0	-2.8316×10^2	0	2.1001×10^2
f_{33}	0	0	0	0	0

and $Li_yNi_{1/3}Co_{1/3}Mn_{1/3}O_2$, respectively. Whilst Levi and Aurbach[77] carried out measurements based on potentiostatic intermittent titration technique (PITT), Wu et al.[27] performed a model based evaluation of measured cell relaxation related to solid phase diffusion. For the diffusion coefficient of Li_xC used within this work, an averaging between data gained from electrodes declared as "thin" and "ultrathin"[77] was performed whilst for the diffusion coefficient of $Li_yNi_{1/3}Co_{1/3}Mn_{1/3}O_2$, an averaging between the behavior of electrodes with two different particle sizes was carried out during both lithiation and delithiation. The fitted behavior is shown in Figs. A1e and A1f (solid black lines) together with the underlying averaged measurement data (black markers). The corresponding fitting functions of $D_{s,\,neg}$ and $D_{s,\,pos}$ (m^2 s^{-1}) are summarized in

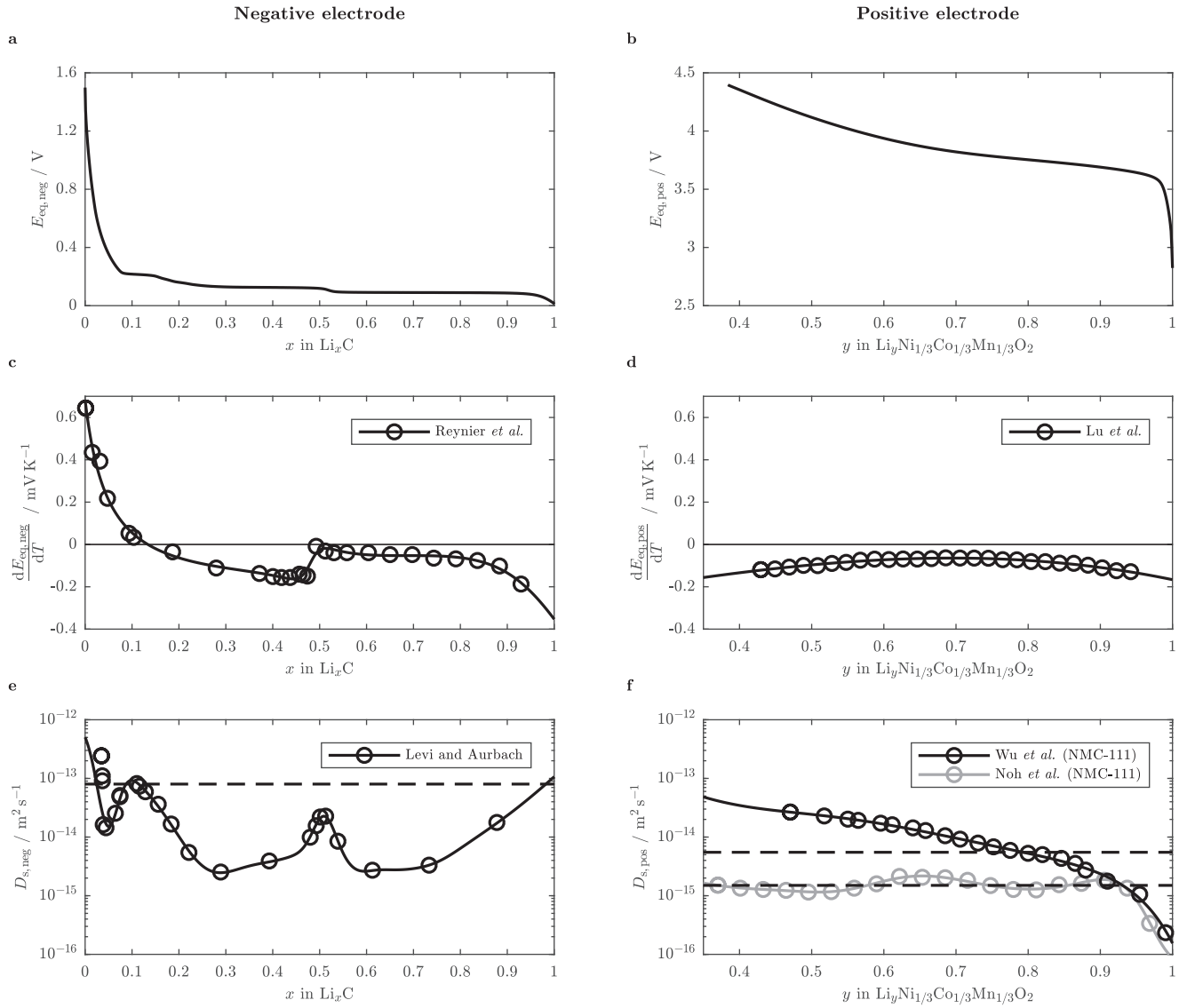

Figure A1. Measured half cell potentials vs. Li/Li$^+$ (top: a and b), fitted entropic coefficients according to experimental data taken from Reynier et al.[70] and Lu et al.[71] (middle: c and d), and fitted Li-ion diffusion coefficients taken from Levi and Aurbach[77] and Wu et al.[27] (bottom: e and f) for the negative (left: a, c, and e) and positive electrode (right: b, d, and f) as a function of degree of lithiation x and y. Markers indicate the considered measurement data. Dashed lines in e and f indicate the used range of effective diffusion coefficients at 25°C. Gray line and markers in f describe reported data from Noh et al.[9] as a comparison.

Eq. A10 and Eq. A11.

$$\begin{aligned}\log_{10} D_{\mathrm{s,\,neg}} = {} & -5.9401{\times}10^{-1}\exp\left(-\left(\frac{x-2.5720{\times}10^{-1}}{8.4006{\times}10^{-2}}\right)^2\right)+\\ & +5.1118{\times}10^{-1}\exp\left(-\left(\frac{x-5.1715{\times}10^{-1}}{1.0308{\times}10^{-1}}\right)^2\right)+\\ & -6.6628{\times}10^{-2}\exp\left(-\left(\frac{x-7.5004{\times}10^{-1}}{6.0470{\times}10^{-2}}\right)^2\right)+\\ & -1.9021{\times}10^{-1}\exp\left(-\left(\frac{x-5.7634{\times}10^{-1}}{4.1183{\times}10^{-2}}\right)^2\right)+\\ & +5.7993{\times}10^{-1}\exp\left(-\left(\frac{x-5.0993{\times}10^{-1}}{3.2647{\times}10^{-2}}\right)^2\right)+\\ & -1.0736{\times}10^{1}\exp\left(-\left(\frac{x-5.5128{\times}10^{-1}}{1.0588}\right)^2\right)+\\ & -1.2463\exp\left(-\left(\frac{x-4.7459{\times}10^{-2}}{3.0551{\times}10^{-2}}\right)^2\right)-4\end{aligned} \qquad [A10]$$

$$\begin{aligned}\log_{10} D_{\mathrm{s,\,pos}} = {} & -1.3922{\times}10^{12}\exp\left(-\left(\frac{y-4.0704}{5.8343{\times}10^{-1}}\right)^2\right)+\\ & -1.4516{\times}10^{1}\exp\left(-\left(\frac{y-1.0490}{1.8016}\right)^2\right)+\\ & -8.6982{\times}10^{-1}\exp\left(-\left(\frac{y-3.0124{\times}10^{-1}}{2.1998{\times}10^{-1}}\right)^2\right)\end{aligned} \qquad [A11]$$

Furthermore, the fitted constant diffusion coefficients used within this work for the negative and positive electrode at 25°C are indicated Figs. A1e and A1f (black dashed lines) and compared to other reported data by Noh et al. for Li$_y$Ni$_{1/3}$Co$_{1/3}$Mn$_{1/3}$O$_2$ (gray solid line and markers in Fig. A1f).

Liquid phase parameters.—In order to complete the set of parameters used within this work, properties characterizing the ionic transport within the liquid electrolyte are required. Accompanied with high currents occurring during short circuit scenarios, large salt concentration gradients are likely to form throughout the electrodes and separator. With a reported significant impact of salt concentration on the inherent transport properties of electrolytes based on $LiPF_6$ and organic solvents such as ionic conductivity κ_l[34,73–76]

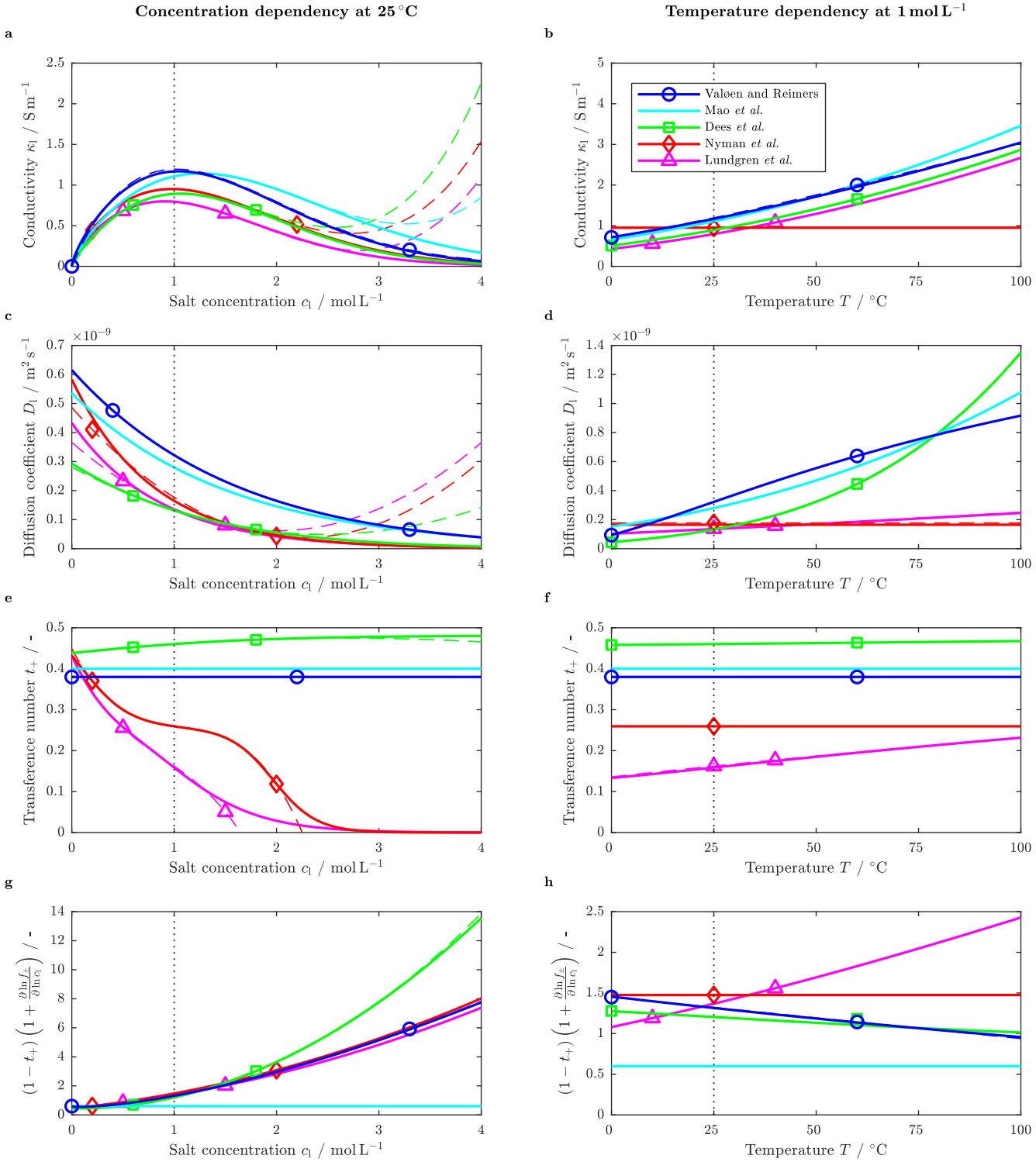

Figure A2. Fitting functions for the ionic conductivity κ_l (a and b), salt diffusion coefficient D_l (c and d), cation transference number t_+ (e and f), and thermodynamic factor TDF (g and h) as a function of the electrolyte's salt concentration c_l at 25°C (left: a, c, e, and g) and as a function of temperature T at 1 mol L^{-1} (right: b, d, f, and h) based on literature from Valøen and Reimers[73] (◯), Mao et al.,[34] Dees et al.[74] (□), Nyman et al.[75] (◊), and Lundgren et al.[76] (△). Markers indicate the considered range of validity.

(S m^{-1}), salt diffusion coefficient D_l[34,73–76] (m^2 s^{-1}), cation transference number t_+ related to the solvent,[74–76] and thermodynamic factor TDF,[73–76] a concentration dependency of these parameters is essential for describing the cell's behavior adequately. Based on the limited concentration range in terms of available data but also in terms of interest for most applications, fitted functions describing transport properties based on salt concentration are often given in a polynomial form which may result e.g. in an increasing κ_l[34,74–76] or D_l[74–76] beyond 3 M, which has not been observed experimentally[73] (see dashed lines in Figs. A2a and A2c). Furthermore, reported fitting functions of decreasing transference numbers[75,76] would even result in negative values at higher concentrations (see dashed lines in Fig. A2e) indicating the presence of negatively-charged clusters dominating ion transport.[94] In order to overcome these issues and to be able to compare the impact of different transport properties on a cell's short circuit behavior at high currents and large concentration gradients, reported fitting functions are re-evaluated and replaced whilst accounting for the reported concentration and temperature dependency.[34,73–76] The adapted

fitting functions are summarized in Table AIII and are shown in Fig. A2 (solid lines) in comparison to the initially reported fitting functions (dashed lines). It is worth stating here, that the initially reported fitting functions for an EC:EMC based electrolyte presented by Dees et al.[74] are based on Gering's advanced electrolyte model.[95] Furthermore, the initially reported fitting functions for both salt diffusion coefficient and transference number of an EC:DEC based electrolyte as discussed by Lundgren et al.[76] are re-evaluated for the temperature range between 25°C and 40°C due to the significantly altered behavior reported at 10°C which differs from the experimental observations made by Valøen and Reimers[73] at lower temperatures.

Acknowledgments

The work presented here was financially supported by the German Federal Ministry of Education and Research (BMBF) under grant number 03XP0027G (*MiBZ*), 03XP0034G (*EffiForm*) and 03XP0081 (*ExZellTUM II*) as well as by the European Union's Horizon 2020 research and innovation program under grant number 713771 (*EVERLASTING*). The authors further thank Marc Steen for his excellent support reviewing this manuscript.

ORCID

Alexander Rheinfeld https://orcid.org/0000-0003-0995-7266
Jörn Wilhelm https://orcid.org/0000-0002-5649-2580
Andreas Jossen https://orcid.org/0000-0003-0964-1405

References

1. N. Nitta, F. Wu, J. T. Lee, and G. Yushin, Li-ion battery materials: present and future, *Materials Today*, **18**, 252 (2015).
2. S. Kosch, A. Rheinfeld, S. V. Erhard, and A. Jossen, An extended polarization model to study the influence of current collector geometry of large-format lithium-ion pouch cells, *Journal of Power Sources*, **342**, 666 (2017).
3. H. Zheng, R. Yang, G. Liu, X. Song, and V. S. Battaglia, Cooperation between Active Material, Polymeric Binder and Conductive Carbon Additive in Lithium Ion Battery Cathode, *The Journal of Physical Chemistry C*, **116**, 4875 (2012).
4. H. Y. Tran, G. Greco, C. Täubert, M. Wohlfahrt-Mehrens, W. Haselrieder, and A. Kwade, Influence of electrode preparation on the electrochemical performance of $LiNi_{0.8}Co_{0.15}Al_{0.05}O_2$composite electrodes for lithium-ion batteries, *Journal of Power Sources*, **210**, 276 (2012).
5. M. Singh, J. Kaiser, and H. Hahn, Thick Electrodes for High Energy Lithium Ion Batteries, *Journal of the Electrochemical Society*, **162**, A1196 (2015).
6. B.-S. Lee, Z. Wu, V. Petrova, X. Xing, H.-D. Lim, H. Liu, and P. Liu, Analysis of Rate-Limiting Factors in Thick Electrodes for Electric Vehicle Applications, *Journal of the Electrochemical Society*, **165**, A525 (2018).
7. C. Campestrini, M. F. Horsche, I. Zilberman, T. Heil, T. Zimmermann, and A. Jossen, Validation and benchmark methods for battery management system functionalities: State of charge estimation algorithms, *Journal of Energy Storage*, **7**, 38 (2016).
8. J. B. Habedank, L. Kraft, A. Rheinfeld, C. Krezdorn, A. Jossen, and M. F. Zaeh, Increasing the Discharge Rate Capability of Lithium-Ion Cells with Laser-Structured Graphite Anodes: Modeling and Simulation, *Journal of the Electrochemical Society*, **165**, A1563 (2018).
9. H.-J. Noh, S. Youn, C. S. Yoon, and Y.-K. Sun, Comparison of the structural and electrochemical properties of layered $Li[Ni_xCo_yMn_z]O_2$(x = 1/3, 0.5, 0.6, 0.7, 0.8 and 0.85) cathode material for lithium-ion batteries, *Journal of Power Sources*, **233**, 121 (2013).
10. S.-M. Bak, K.-W. Nam, W. Chang, X. Yu, E. Hu, S. Hwang, E. A. Stach, K.-B. Kim, K. Y. Chung, and X.-Q. Yang, Correlating Structural Changes and Gas Evolution during the Thermal Decomposition of Charged $Li_xNi_{0.8}Co_{0.15}Al_{0.05}O_2$Cathode Materials, *Chemistry of Materials*, **25**, 337 (2013).
11. L. Ma, M. Nie, J. Xia, and J. R. Dahn, A systematic study on the reactivity of different grades of charged $Li[Ni_xMn_yCo_z]O_2$with electrolyte at elevated temperatures using accelerating rate calorimetry, *Journal of Power Sources*, **327**, 145 (2016).
12. A. Rheinfeld, A. Noel, J. Wilhelm, A. Kriston, A. Pfrang, and A. Jossen, Quasi-Isothermal External Short Circuit Tests Applied to Lithium-Ion Cells: Part I. Measurements, *Journal of The Electrochemical Society*, **165**, A3427 (2018).
13. Y.-S. Park and S.-M. Lee, Effects of particle size on the thermal stability of lithiated graphite anode, *Electrochimica Acta*, **54**, 3339 (2009).
14. J. Geder, H. E. Hoster, A. Jossen, J. Garche, and D. Y. Yu, Impact of active material surface area on thermal stability of $LiCoO_2$ cathode, *Journal of Power Sources*, **257**, 286 (2014).
15. H. Zheng, J. Li, X. Song, G. Liu, and V. S. Battaglia, A comprehensive understanding of electrode thickness effects on the electrochemical performances of Li-ion battery cathodes, *Electrochimica Acta*, **71**, 258 (2012).
16. N. Ogihara, Y. Itou, T. Sasaki, and Y. Takeuchi, Impedance Spectroscopy Characterization of Porous Electrodes under Different Electrode Thickness Using a Symmetric Cell for High-Performance Lithium-Ion Batteries, *The Journal of Physical Chemistry C*, **119**, 4612 (2015).
17. K. J. Lee, W. Bak, J.-J. Kim, M. A. Snyder, W. C. Yoo, and Y.-E. Sung, How Pore Parameters Affect Li Ion Depletion in Mesoporous Materials for Lithium-Ion Batteries, *The Journal of Physical Chemistry C*, **119**, 7604 (2015).
18. K. Kitada, H. Murayama, K. Fukuda, H. Arai, Y. Uchimoto, Z. Ogumi, and E. Matsubara, Factors determining the packing-limitation of active materials in the composite electrode of lithium-ion batteries, *Journal of Power Sources*, **301**, 11 (2016).
19. F. Jiang and P. Peng, Elucidating the Performance Limitations of Lithium-ion Batteries due to Species and Charge Transport through Five Characteristic Parameters, *Scientific reports*, **6**, 32639 (2016).
20. T. Danner, M. Singh, S. Hein, J. Kaiser, H. Hahn, and A. Latz, Thick electrodes for Li-ion batteries: A model based analysis, *Journal of Power Sources*, **334**, 191 (2016).
21. Z. Du, D. L. Wood, C. Daniel, S. Kalnaus, and J. Li, Understanding limiting factors in thick electrode performance as applied to high energy density Li-ion batteries, *Journal of Applied Electrochemistry*, **47**, 405 (2017).
22. S. T. Taleghani, B. Marcos, K. Zaghib, and G. Lantagne, A Study on the Effect of Porosity and Particles Size Distribution on Li-Ion Battery Performance, *Journal of the Electrochemical Society*, **164**, E3179 (2017).
23. M. Doyle, J. Newman, A. S. Gozdz, C. N. Schmutz, and J.-M. Tarascon, Comparison of Modeling Predictions with Experimental Data from Plastic Lithium Ion Cells, *Journal of The Electrochemical Society*, **143**, 1890 (1996).
24. P. Arora, M. Doyle, A. S. Gozdz, R. E. White, and J. Newman, Comparison between computer simulations and experimental data for high-rate discharges of plastic lithium-ion batteries, *Journal of Power Sources*, **88**, 219 (2000).
25. K. Smith and C.-Y. Wang, Solid-state diffusion limitations on pulse operation of a lithium ion cell for hybrid electric vehicles, *Journal of Power Sources*, **161**, 628 (2006).
26. A. Nyman, T. G. Zavalis, R. Elger, M. Behm, and G. Lindbergh, Analysis of the Polarization in a Li-Ion Battery Cell by Numerical Simulations, *Journal of The Electrochemical Society*, **157**, A1236 (2010).
27. S.-L. Wu, W. Zhang, X. Song, A. K. Shukla, G. Liu, V. Battaglia, and V. Srinivasan, High Rate Capability of $Li(Ni_{1/3}Mn_{1/3}Co_{1/3})O_2$Electrode for Li-Ion Batteries, *Journal of the Electrochemical Society*, **159**, A438 (2012).
28. J. N. Reimers, M. Shoesmith, Y. S. Lin, and L. O. Valoen, Simulating High Current Discharges of Power Optimized Li-Ion Cells, *Journal of the Electrochemical Society*, **160**, A1870 (2013).
29. R. Zhao, J. Liu, and J. Gu, The effects of electrode thickness on the electrochemical and thermal characteristics of lithium ion battery, *Applied Energy*, **139**, 220 (2015).
30. K. G. Gallagher, S. E. Trask, C. Bauer, T. Woehrle, S. F. Lux, M. Tschech, P. Lamp, B. J. Polzin, S. Ha, B. Long, Q. Wu, W. Lu, D. W. Dees, and A. N. Jansen, Optimizing Areal Capacities through Understanding the Limitations of Lithium-Ion Electrodes, *Journal of The Electrochemical Society*, **163**, A138 (2015).
31. S. Malifarge, B. Delobel, and C. Delacourt, Experimental and Modeling Analysis of Graphite Electrodes with Various Thicknesses and Porosities for High-Energy-Density Li-Ion Batteries, *Journal of the Electrochemical Society*, **165**, A1275 (2018).
32. A. Kriston, A. Pfrang, H. Döring, B. Fritsch, V. Ruiz, I. Adanouj, T. Kosmidou, J. Ungeheuer, and L. Boon-Brett, External short circuit performance of Graphite-$LiNi_{1/3}Co_{1/3}Mn_{1/3}O_2$and Graphite-$LiNi_{0.8}Co_{0.15}Al_{0.05}O_2$ cells at different external resistances, *Journal of Power Sources*, **361**, 170 (2017).
33. J. Mao, W. Tiedemann, and J. Newman, Simulation of Li-ion Cells by Dualfoil Model under Constant-Resistance Load, *ECS Transactions*, **58**, 71 (2014).
34. J. Mao, W. Tiedemann, and J. Newman, Simulation of temperature rise in Li-ion cells at very high currents, *Journal of Power Sources*, **271**, 444 (2014).
35. D. J. Noelle, M. Wang, A. V. Le, Y. Shi, and Y. Qiao, Internal resistance and polarization dynamics of lithium-ion batteries upon internal shorting, *Applied Energy*, **212**, 796 (2018).
36. C. J. Orendorff, E. P. Roth, and G. Nagasubramanian, Experimental triggers for internal short circuits in lithium-ion cells, *Journal of Power Sources*, **196**, 6554 (2011).
37. J. Lamb and C. J. Orendorff, Evaluation of mechanical abuse techniques in lithium ion batteries, *Journal of Power Sources*, **247**, 189 (2014).
38. T. D. Hatchard, S. Trussler, and J. R. Dahn, Building a "smart nail" for penetration tests on Li-ion cells, *Journal of Power Sources*, **247**, 821 (2014).
39. M. Zhang, J. Du, L. Liu, A. Stefanopoulou, J. Siegel, L. Lu, X. He, X. Xie, and M. Ouyang, Internal Short Circuit Trigger Method for Lithium-Ion Battery Based on Shape Memory Alloy, *Journal of The Electrochemical Society*, **164**, A3038 (2017).
40. S. Santhanagopalan, P. Ramadass, and J. Zhang, Analysis of internal short-circuit in a lithium ion cell, *Journal of Power Sources*, **194**, 550 (2009).
41. T. G. Zavalis, M. Behm, and G. Lindbergh, Investigation of Short-Circuit Scenarios in a Lithium-Ion Battery Cell, *Journal of The Electrochemical Society*, **159**, A848 (2012).
42. W. Zhao, G. Luo, and C.-Y. Wang, Modeling Nail Penetration Process in Large-Format Li-Ion Cells, *Journal of The Electrochemical Society*, **162**, A207 (2015).
43. W. Zhao, G. Luo, and C.-Y. Wang, Modeling Internal Shorting Process in Large-Format Li-Ion Cells, *Journal of The Electrochemical Society*, **162**, A1352 (2015).
44. H. Maleki and J. N. Howard, Internal short circuit in Li-ion cells, *Journal of Power Sources*, **191**, 568 (2009).
45. W. Fang, P. Ramadass, and Z. Zhang, Study of internal short in a Li-ion cell-II. Numerical investigation using a 3D electrochemical-thermal model, *Journal of Power Sources*, **248**, 1090 (2014).
46. K.-C. Chiu, C.-H. Lin, S.-F. Yeh, Y.-H. Lin, and K.-C. Chen, An electrochemical modeling of lithium-ion battery nail penetration, *Journal of Power Sources*, **251**, 254 (2014).

47. R. Zhao, J. Liu, and J. Gu, Simulation and experimental study on lithium ion battery short circuit, *Applied Energy*, **173**, 29 (2016).
48. B. Liu, S. Yin, and J. Xu, Integrated computation model of lithium-ion battery subject to nail penetration, *Applied Energy*, **183**, 278 (2016).
49. M. Zhang, L. Liu, A. Stefanopoulou, J. Siegel, L. Lu, X. He, and M. Ouyang, Fusing Phenomenon of Lithium-Ion Battery Internal Short Circuit. *Journal of The Electrochemical Society*, **164**, A2738 (2017).
50. J. Xu, Y. Wu, and S. Yin, Investigation of effects of design parameters on the internal short-circuit in cylindrical lithium-ion batteries, *RSC Advances*, **7**, 14360 (2017).
51. G. Liang, Y. Zhang, Q. Han, Z. Liu, Z. Jiang, and S. Tian, A novel 3D-layered electrochemical-thermal coupled model strategy for the nail-penetration process simulation, *Journal of Power Sources*, **342**, 836 (2017).
52. P. T. Coman, E. C. Darcy, C. T. Veje, and R. E. White, Modelling Li-Ion Cell Thermal Runaway Triggered by an Internal Short Circuit Device Using an Efficiency Factor and Arrhenius Formulations, *Journal of The Electrochemical Society*, **164**, A587 (2017).
53. X. Feng, X. He, L. Lu, and M. Ouyang, Analysis on the Fault Features for Internal Short Circuit Detection Using an Electrochemical-Thermal Coupled Model, *Journal of The Electrochemical Society*, **165**, A155 (2018).
54. J. Zhu, T. Wierzbicki, and W. Li, A review of safety-focused mechanical modeling of commercial lithium-ion batteries, *Journal of Power Sources*, **378**, 153 (2018).
55. R. Spotnitz and J. Franklin, Abuse behavior of high-power, lithium-ion cells, *Journal of Power Sources*, **113**, 81 (2003).
56. S. Pannala, J. A. Turner, S. Allu, W. R. Elwasif, S. Kalnaus, S. Simunovic, A. Kumar, J. J. Billings, H. Wang, and J. Nanda, Multiscale modeling and characterization for performance and safety of lithium-ion batteries, *Journal of Applied Physics*, **118**, 072017 (2015).
57. S. Abada, G. Marlair, A. Lecocq, M. Petit, V. Sauvant-Moynot, and F. Huet, Safety focused modeling of lithium-ion batteries: A review, *Journal of Power Sources*, **306**, 178 (2016).
58. J. Deng, C. Bae, J. Marcicki, A. Masias, and T. Miller, Safety modeling and testing of lithium-ion batteries in electrified vehicles, *Nature Energy*, **3**, 261 (2018).
59. M. Doyle, T. F. Fuller, and J. Newman, Modeling of Galvanostatic Charge and Discharge of the Lithium/Polymer/Insertion Cell, *Journal of The Electrochemical Society*, **140**, 1526 (1993).
60. J. Newman and K. E. Thomas-Alyea, *Electrochemical Systems*, 3rd ed., Wiley-Interscience: s.l., 2004.
61. T. J. Rademaker, G. R. A. Akkermans, D. L. Danilov, and P. H. L. Notten, On the Deviation of Electro-Neutrality in Li-Ion Battery Electrolytes, *Journal of The Electrochemical Society*, **161**, E3365 (2014).
62. K.-H. Xue and G. L. Plett, A convective transport theory for high rate discharge in lithium ion cells, *Electrochimica Acta*, **87**, 575 (2013).
63. T. D. Hatchard, D. D. MacNeil, A. Basu, and J. R. Dahn, Thermal Model of Cylindrical and Prismatic Lithium-Ion Cells, *Journal of The Electrochemical Society*, **148**, A755 (2001).
64. S. Hildebrand, A. Rheinfeld, A. Friesen, J. Haetge, F. M. Schappacher, A. Jossen, and M. Winter, Thermal Analysis of $LiNi_{0.4}Co_{0.2}Mn_{0.4}O_2$/Mesocarbon Microbeads Cells and Electrodes: State-of-Charge and State-of-Health Influences on Reaction Kinetics, *Journal of The Electrochemical Society*, **165**, A104 (2018).
65. T. F. Fuller, M. Doyle, and J. Newman, Simulation and Optimization of the Dual Lithium Ion Insertion Cell, *Journal of The Electrochemical Society*, **141**, 1 (1994).
66. A. Latz and J. Zausch, Thermodynamic derivation of a Butler–Volmer model for intercalation in Li-ion batteries, *Electrochimica Acta*, **110**, 358 (2013).
67. C. H. Hamann, A. Hamnett, and W. Vielstich, *Electrochemistry*, Wiley-VCH: Weinheim, 2007.
68. D. Bernardi, E. Pawlikowski, and J. Newman, A General Energy Balance for Battery Systems, *Journal of The Electrochemical Society*, **132**, 5 (1985).
69. L. Rao and J. Newman, Heat-Generation Rate and General Energy Balance for Insertion Battery Systems, *Journal of The Electrochemical Society*, **144**, 2697 (1997).
70. Y. Reynier, R. Yazami, and B. Fultz, The entropy and enthalpy of lithium intercalation into graphite, *Journal of Power Sources*, **119-121**, 850 (2003).
71. W. Lu, I. Belharouak, D. Vissers, and K. Amine, In Situ Thermal Study of $Li_{1+x}(Ni_{1/3}Co_{1/3}Mn_{1/3})_{1-x}O_2$Using Isothermal Micro-clorimetric Techniques, *Journal of The Electrochemical Society*, **153**, A2147 (2006).
72. S. V. Erhard et al., Simulation and Measurement of the Current Density Distribution in Lithium-Ion Batteries by a Multi-Tab Cell Approach, *Journal of The Electrochemical Society*, **164**, A6324 (2017).
73. L. O. Valøen and J. N. Reimers, Transport Properties of $LiPF_6$-Based Li-Ion Battery Electrolytes, *Journal of The Electrochemical Society*, **152**, A882 (2005).
74. D. Dees, E. Gunen, D. Abraham, A. Jansen, and J. Prakash, Electrochemical Modeling of Lithium-Ion Positive Electrodes during Hybrid Pulse Power Characterization Tests, *Journal of The Electrochemical Society*, **155**, A603 (2008).
75. A. Nyman, M. Behm, and G. Lindbergh, Electrochemical characterisation and modeling of the mass transport phenomena in $LiPF_6$–EC–EMC electrolyte, *Electrochimica Acta*, **53**, 6356 (2008).
76. H. Lundgren, M. Behm, and G. Lindbergh, Electrochemical Characterization and Temperature Dependency of Mass-Transport Properties of $LiPF_6$in EC: DEC, *Journal of the Electrochemical Society*, **162**, A413 (2014).
77. M. D. Levi and D. Aurbach, Diffusion Coefficients of Lithium Ions during Intercalation into Graphite Derived from the Simultaneous Measurements and Modeling of Electrochemical Impedance and Potentiostatic Intermittent Titration Characteristics of Thin Graphite Electrodes, *The Journal of Physical Chemistry B*, **101**, 4641 (1997).
78. J. Landesfeind, J. Hattendorff, A. Ehrl, W. A. Wall, and H. A. Gasteiger, Tortuosity Determination of Battery Electrodes and Separators by Impedance Spectroscopy, *Journal of The Electrochemical Society*, **163**, A1373 (2016).
79. M. Winter, J. O. Besenhard, M. E. Spahr, and P. Novák, Insertion Electrode Materials for Rechargeable Lithium Batteries, *Advanced Materials*, **10**, 725 (1998).
80. A. Latz and J. Zausch, Multiscale modeling of lithium ion batteries: Thermal aspects, *Beilstein journal of nanotechnology*, **6**, 987 (2015).
81. K. Higa, S.-L. Wu, D. Y. Parkinson, Y. Fu, S. Ferreira, V. Battaglia, and V. Srinivasan, Comparing Macroscale and Microscale Simulations of Porous Battery Electrodes, *Journal of The Electrochemical Society*, **164**, E3473 (2017).
82. R. Darling and J. Newman, Modeling a Porous Intercalation Electrode with Two Characteristic Particle Sizes, *Journal of The Electrochemical Society*, **144**, 4201 (1997).
83. M. Ender, An extended homogenized porous electrode model for lithium-ion cell electrodes, *Journal of Power Sources*, **282**, 572 (2015).
84. Z. Mao, M. Farkhondeh, M. Pritzker, M. Fowler, and Z. Chen, Multi-Particle Model for a Commercial Blended Lithium-Ion Electrode, *Journal of the Electrochemical Society*, **163**, A458 (2015).
85. C. Kupper and W. G. Bessler, Multi-Scale Thermo-Electrochemical Modeling of Performance and Aging of a $LiFePO_4$ /Graphite Lithium-Ion Cell, *Journal of The Electrochemical Society*, **164**, A304 (2017).
86. D. A. G. Bruggeman, Berechnung verschiedener physikalischer Konstanten von heterogenen Substanzen. I. Dielektrizitätskonstanten und Leitfähigkeiten der Mischkörper aus isotropen Substanzen, *Annalen der Physik*, **416**, 636 (1935).
87. E. Markevich, M. D. Levi, and D. Aurbach, Comparison between potentiostatic and galvanostatic intermittent titration techniques for determination of chemical diffusion coefficients in ion-insertion electrodes, *Journal of Electroanalytical Chemistry*, **580**, 231 (2005).
88. S. Malifarge, B. Delobel, and C. Delacourt, Guidelines for the Analysis of Data from the Potentiostatic Intermittent Titration Technique on Battery Electrodes, *Journal of The Electrochemical Society*, **164**, A3925 (2017).
89. K. R. Crompton and B. J. Landi, Opportunities for near zero volt storage of lithium ion batteries, *Energy & Environmental Science*, **9**, 2219 (2016).
90. G. E. Archie, The Electrical Resistivity Log as an Aid in Determining Some Reservoir Characteristics, *Transactions of the AIME*, **146**, 54 (1942).
91. J. Sturm, A. Rheinfeld, I. Zilberman, F. B. Spingler, S. Kosch, F. Frie, and A. Jossen, Modeling and simulation of inhomogeneities in a 18650 nickel-rich, silicon-graphite lithium-ion cell during fast charging, *Journal of Power Sources*, **412**, 204 (2019).
92. S. V. Erhard, P. J. Osswald, J. Wilhelm, A. Rheinfeld, S. Kosch, and A. Jossen, Simulation and Measurement of Local Potentials of Modified Commercial Cylindrical Cells, *Journal of The Electrochemical Society*, **162**, A2707 (2015).
93. K. E. Thomas and J. Newman, Heats of mixing and of entropy in porous insertion electrodes, *Journal of Power Sources*, **119-121**, 844 (2003).
94. D. M. Pesko, K. Timachova, R. Bhattacharya, M. C. Smith, I. Villaluenga, J. Newman, and N. P. Balsara, Negative Transference Numbers in Poly(ethylene oxide)-Based Electrolytes. *Journal of The Electrochemical Society*, **164**, E3569 (2017).
95. K. L. Gering, Prediction of electrolyte viscosity for aqueous and non-aqueous systems: Results from a molecular model based on ion solvation and a chemical physics framework, *Electrochimica Acta*, **51**, 3125 (2006).
96. T. Marks, S. Trussler, A. J. Smith, D. Xiong, and J. R. Dahn, A Guide to Li-Ion Coin-Cell Electrode Making for Academic Researchers, *Journal of The Electrochemical Society*, **158**, A51 (2011).